Flagellar dynamics reveal fluctuations and kinetic limit in the *Escherichia coli* chemotaxis network

Roshni Bano[1,3], Patrick Mears[2,3], Ido Golding[1,2,3], Yann R. Chemla[1,2,3,*]

[1]*Center for Biophysics and Quantitative Biology, University of Illinois, Urbana-Champaign*

[2]*Department of Physics, University of Illinois, Urbana-Champaign*

[3]*Center for the Physics of Living Cells, University of Illinois, Urbana-Champaign*

*For correspondence: ychemla@illinois.edu

Abstract

Biochemical signaling networks allow living cells to adapt to a changing environment, but these networks must cope with unavoidable number fluctuations ("noise") in their molecular constituents. *Escherichia coli* chemotaxis, by which bacteria modulate their random run/tumble swimming pattern to navigate their environment, is a paradigm for the role of noise in cell signaling. The key signaling protein, CheY, when activated by (reversible) phosphorylation, causes a switch in the rotational direction of the flagellar motors propelling the cell, leading to tumbling. CheY-P concentration, [CheY-P], is thus a measure of the chemotaxis network's output, and temporal fluctuations in [CheY-P] provide a proxy for network noise. Here we quantify the fluctuations in [CheY-P] from the switching dynamics of individual flagella, observed using time-resolved fluorescence microscopy of optically trapped *E. coli* cells. This approach reveals [CheY-P] fluctuations at steady state, which may play a critical role in driving flagellar switching and cell tumbling. A stochastic theoretical model, inspired by work on gene expression noise, points to CheY activation occurring in bursts, driving the [CheY-P] fluctuations. When the network is stimulated chemically to higher activity, we observe a dramatic decrease in [CheY-P] fluctuations. Our stochastic model shows that an intrinsic kinetic ceiling on network activity places an upper limit on [CheY-P], which when encountered suppresses its fluctuations. This limit may also prevent cells from tumbling unproductively in steep gradients.

Introduction

A common feature of living organisms is their ability to sense environmental signals and respond to these signals by modifying their behavior. This ability is enabled by signal transduction, which converts environmental inputs into behavioral outputs[1]. Studies have shown that signaling networks must operate in the presence of noise not only in their inputs but also in the circuit components themselves[2,3]. Until recently, it was thought that signaling networks had evolved to be robust against undesirable noise[4–7]. More recent studies have shifted to understanding the role of noise in regulating and fine-tuning biological function[8,9]. For example, noise resulting from transcription/translation has been measured precisely and shown to play a critical role in networks for gene expression and regulation[10–12]. In contrast, studying noise resulting from signaling networks at the post-translation level has proven more challenging.

One extensively studied signaling system is the chemotaxis network of *E. coli*, which cells use to navigate their environment[13–17]. *E. coli* cells swim in a random walk consisting of "runs"—during which their flagella rotate counter-clockwise (CCW)—and "tumbles"—during which one or more flagella rotate clockwise (CW)[18–21]. Changing environmental conditions are sensed through a two-component signaling system comprising receptors that bind extracellular ligands and a kinase, CheA, that transfers its phosphoryl group onto downstream effectors[22]. The response regulator, CheY, when phosphorylated by the receptor kinase complex to CheY-P, binds to the flagellar motor and increases the probability of CW motor rotation[23–25]. The phosphatase CheZ carries out the opposite reaction, maintaining a dynamic equilibrium between CheY and CheY-P (**Figure 1a**)[26,27]. Additionally, the methyltransferase CheR and the methylesterase CheB covalently modify receptors, and the resulting modulation of CheA activity affects CheY-P levels over the timescales of chemotactic adaptation[28–30]. While the population averaged relationships between these signaling protein concentrations and cellular motility in *E. coli* are now well understood[13–16,24], the role of fluctuations in protein concentrations in modulating cell behavior remains comparatively unexplored.

The intracellular CheY-P concentration, [CheY-P], is a dynamic indicator of the cell's environment and determines its trajectory of motion. Thus, [CheY-P] fluctuations are the primary indicator of noise upstream in the signaling network and affect downstream behavior. Cluzel et

al. [25] showed that the motor CW bias, the probability of CW rotation of a single flagellar motor, has an ultrasensitive switch-like dependence on the intracellular [CheY-P]. Thus, the cell's swimming behavior is sensitive to small temporal fluctuations in [CheY-P] (**Figure 1b, i-iii**). Noise due to CheY-P fluctuations was first inferred by Korobkova et al.[31] from long-term measurements of individual rotating flagellar motors, where larger-than-expected noise in the motor CW bias was attributed to methylation/demethylation dynamics of CheR/CheB over long timescales (10s of seconds). Recently, single-cell measurements probing intracellular [CheY-P] using fluorescent reporters revealed a potential new source of noise arising from the dynamics of the receptor kinase complex itself[32,33]. Noise in the *E. coli* chemotaxis signaling network is thought to have functional consequences for sensing and navigation in complex natural microenvironments. It has been proposed to allow cells to sample 3D space more effectively[31,34], enhance chemotactic drift up a gradient[35–37], and synchronize flagellar switching to mitigate differences in swimming behavior among cells with different numbers of flagella[38,39].

Here, we use optical trapping coupled with time-resolved fluorescence microscopy[39,40] to infer temporal [CheY-P] fluctuations from the statistics of flagellar switching in individual multi-flagellated *E. coli* cells. In contrast to fluorescence-based approaches that provide a relative measure of noise[32,33], here it is measured directly in terms of CheY-P concentration fluctuations. Analyzing cells at steady state, we determine the single-cell distribution of [CheY-P], which reveals that the network is poised at a low CW bias, favoring CCW flagellar rotation/running, and that transient fluctuations in [CheY-P] drive CW flagellar rotation/tumbling. Unlike previous studies where fluctuations were studied over long timescales (>10 s)[31–33,41], our method measures fluctuations at the timescales of individual runs and tumbles (0.5-5 s), which allows us to track the time evolution of signaling noise in cells undergoing adaptation. We find that fluctuations are significantly reduced upon applying a stimulus that increases CheA activity. A simple stochastic model in which noise in signaling arises from large, burst-like fluctuations in CheA activity recapitulates all of our experimental results and suggests that the decrease in CheY-P fluctuations upon stimulation is due to a kinetic ceiling on the CheA activity.

Results

86 **Flagellar switching statistics reveal temporal [CheY-P] fluctuations**

87 We inferred the temporal fluctuations in the intracellular CheY-P concentration from the
88 dynamics of flagellar switching in individual cells. We imaged fluorescently labeled flagella on
89 individual, swimming cells to determine their CCW/CW rotation state, using an optical trapping
90 assay described previously[39,40,42] (see **Materials and Methods**). Briefly, *E. coli* cells were injected
91 into a laminar flow chamber containing two parallel channels. A single cell was captured using a
92 dual beam optical trap from one channel containing many cells (labeled "cells" in **Figure 1c**) and
93 moved for observation to a second channel containing no other cells (labeled "blank" in **Figure**
94 **1c**). The light scattered by the optically trapped cell was used to monitor the run/tumble
95 swimming behavior as described previously (data not shown, see Ref. [40]). Simultaneously, high-
96 speed, epi-fluorescent stroboscopic imaging[39] was used to monitor the rotation state of all the
97 individual flagella on the cell at high temporal resolution (0.1 s) and long-time duration (typically
98 ~15-40 s, until the flagella photobleached) (**Figure 1d,** top). Following Darnton et al.[21] and our
99 previous work[39], the CCW/CW rotation state of each flagellum was visually identified by its
100 different helical waveforms (see **Materials and Methods**).

101 We next inferred the distribution of [CheY-P], making use of the statistics of switching in
102 multi-flagellated cells. For a cell with N flagellar motors, the probability that n_{cw} rotate in a CW
103 direction, $p_N(n_{cw})$, is equal to (see **Materials and Methods**):

104 $$p_N(n_{cw}) = \int_0^1 dc\, p_N(n_{cw} \mid c) p(c), \tag{1}$$

105 where c is the instantaneous motor CW bias, or probability that any one motor is CW, $p_N(n_{cw} \mid c)$
106 is the conditional probability that n_{cw} out of N motors are in the CW state given a certain c, and
107 $p(c)$ is the distribution of CW biases (**Figure 1b, iii**). Given the finding that flagellar motors switch
108 independently of each other[39], $p_N(n_{cw} \mid c)$ is given by the binomial distribution:

109 $$p_N(n_{cw} \mid c) = \binom{N}{n_{cw}} c^{n_{cw}} (1-c)^{N-n_{cw}}. \tag{2}$$

110 Transitions between CW and CCW flagellar rotation are engendered by a switch complex at
111 the base of each motor that binds CheY-P with high cooperativity. The motor CW bias c depends

112 on the intracellular CheY-P concentration in a switch-like manner, customarily modeled by a
113 sigmoidal Hill equation (**Figure 1b, ii**)[25]:

114 $$c(y_P) = \frac{y_P^H}{K^H + y_P^H}\,, \tag{3}$$

115 where $y_P \equiv$ [CheY-P], K is the CheY-P concentration at 0.5 CW bias, and H is the Hill coefficient.
116 (Analytical forms for $c(y_P)$ other than Eq. (3) are also commonly used[43], and are indistinguishable
117 in shape; see **Appendix**). For simplicity, we adopted the Hill equation, Eq. (3), in our analysis).
118 Thus, Eq. (1) for $p_N(n_{cw})$ can be written in terms of [CheY-P]:

119 $$p_N(n_{cw}) = \int_0^{y_{\text{tot}}} dy_P\; p_N(n_{cw} \mid y_P) p(y_P)\,, \tag{4}$$

120 where y_{tot} is the total intracellular CheY concentration, reported to be ~10 μM for cells under
121 growth conditions similar to ours[44] (see **Materials and Methods**). $p(y_P)$ is the distribution of
122 [CheY-P] (**Figure 1b, i**), and the conditional probability $p_N(n_{cw} \mid y_P)$ is obtained by combining Eq.
123 (2) and (3) to yield:

124 $$p_N(n_{cw} \mid y_P) = \binom{N}{n_{cw}} \frac{y_P^{n_{cw}H}}{(K^H + y_P^H)^N}\,. \tag{5}$$

125 Since the conditional probability is known, Eq. (4) in principle allows one to connect the
126 probability $p_N(n_{cw})$—which can be determined from measurements of the CCW/CW rotational
127 state of each flagellum of a cell with N flagellar motors—to the distribution of [CheY-P], $p(y_P)$.
128 (Eq. (1) can similarly be used to connect to the distribution of CW biases $p(c)$). In practice,
129 solutions to Eqs. (1) and (4) are not unique, but one can show that an increasing number of
130 moments of the distribution $p(c)$ are determined as N increases (see **Materials and Methods**).
131 Thus, one expects that the distribution $p(c)$, and thus the distribution $p(y_P)$ which captures
132 fluctuations in [CheY-P], can be estimated over a given time window with increasing accuracy as
133 N increases. Essentially, since each flagellar motor independently measures the intracellular level
134 of CheY-P, the more motors a cell possesses, the better our estimate of the mean [CheY-P] and
135 its fluctuations.

We note that while $p(c)$ is determined exactly from Eq. (1) with no additional input parameters, $p(y_P)$ requires values for the parameters H, K, and y_{tot} in Eqs. (4) and (5). In particular, $p(y_P)$ depends non-negligibly on K and H (see **Appendix** for a detailed discussion on the sensitivity to K and H). Initial single-cell measurements of the motor c vs. y_P response function[25] yielded values of H = 10.3 and K = 3.1 μM. However, the discovery of remodeling in the flagellar motor[45–47]—which causes the number of FliM, the component of the motor switch complex that binds CheY-P, to vary according to intracellular CheY-P levels—has led to revised estimates of the Hill coefficient, $H \sim 20$, nearly twice as large[47]. Furthermore, remodeling causes the motor response function to shift depending on CheY-P level, such that K (and to a lesser extent H) depend on the steady-state CW bias of the motor[43,45] (see **Appendix** for a discussion on remodeling). As detailed below, we account for the effect of motor remodeling in determining the appropriate values of K and H in Eqs. (4) and (5) given the CW bias of the cell. We also note that, since y_P is determined only relative to K, we plot and report values for the ratio y_P/K, which is the functionally important parameter for *E. coli* chemotaxis. In contrast to K and H, $p(y_P)$ is insensitive to the exact value of y_{tot}, because the CW bias $c \approx 1$ when $y_P = y_{\mathrm{tot}} > K$ according to Eq. (3). (The upper limit for the integral in Eq. (4) can be replaced with ∞ with error <0.01%). Lastly we note that writing Eqs. (4) and (5) implicitly assumes that the motor response function, $c(y_P)$, is identical for all motors. An analysis of the CW bias across motors and cells indicates that this variability is negligible, and justifies our use of a single value for K and for H across all cells (see **Appendix** for further discussion).

Figure 1 shows the workflow to determine $p(y_P)$ experimentally. Fluorescence tracking of the CCW/CW state of the individual flagella (**Figure 1d,** middle) is represented as a time trace of the number of CW flagella (**Figure 1d,** bottom). For a cell with N flagella, a histogram of this time trace was used to construct the probability distribution $p_N(n_{cw})$ that n_{cw} out of N flagella rotate CW (**Figure 1e**, bottom**,** histogram). We determined the probability distributions $p(c)$ (**Figure 1e**, middle) and $p_{fit}(y_P)$ (**Figure 1e**, top) via the integral equations Eqs. (1) and (4), respectively, using a trial distribution function and finding the parameters that generated the probability distribution $p_{N,fit}(n_{cw})$ (**Figure 1e**, bottom, solid line) that best fitted the experimental distribution

164 (see **Materials and Methods**). Below we show the results of this analysis for one choice of trial
165 distribution function (see **Materials and Methods** for a discussion on alternate choices).
166
167 **The chemotaxis network exhibits [CheY-P] fluctuations at steady-state**
168 We first applied the above approach to free-swimming (i.e. unstimulated) cells for which the
169 chemotaxis network is in a steady state. Fluorescence tracking data of CCW/CW flagellar states
170 were obtained for cells of a strain wild-type for chemotaxis (HCB1660, henceforth referred to as
171 "wild-type"; see **Materials and Methods**) with N = 2 to 5 flagella. Data traces tracking n_{cw} were
172 pooled together from multiple cells with the same total number of flagella N to generate $p_N(n_{cw})$
173 (**Figure 2a**, colored histograms). As we show below, pooling over the population of cells did not
174 affect our results appreciably.
175 Since we did not expect the number of flagella to have an effect on fluctuations of the
176 underlying network, we fitted the data globally, determining a single CW bias and [CheY-P]
177 distribution for all values of N. The best global motor bias distribution $p_{glofit}(c)$ is shown in **Figure**
178 **2b**, determined using the beta distribution as a trial function (see **Materials and Methods**; Eq.
179 (15)). The corresponding distributions of number of CW flagella, $p_{N,glofit}(n_{cw})$, are shown in **Figure**
180 **2a** (gray solid lines). The mean and standard deviation in CW bias from this global fit were $\mu_{c,glo}$ =
181 0.14 ± 0.02 and $\sigma_{c,glo}$ = 0.22 ± 0.02, respectively. Given the above mean CW bias value, we used a
182 quantitative model by Zhang et al.[43] for FliM remodeling dynamics in the motor switch complex
183 to determine that K = 2.4 μM and H = 18 for the motor c vs y_P response function, Eq. (3) (see
184 **Appendix**). Given these values of K and H, we determined from $p_{glofit}(c)$ and Eq. (10) the
185 corresponding best fit global [CheY-P] distribution $p_{glofit}(y_P)$, shown in **Figure 2c** (gray solid curve;
186 see **Materials and Methods**). The mean and standard deviation of [CheY-P] relative to the
187 parameter K from this global fit were $\mu_{y_P,glo}/K$ = 0.80 ± 0.03 and $\sigma_{y_P,glo}/K$ = 0.18 ± 0.03, respectively.
188 **Figure 2 – figure supplement 1** shows the estimated error in the best fit [CheY-P] distributions,
189 as determined by bootstrap resampling (see **Materials and Methods**). Alternate choices of trial
190 functions for the fitting distributions did not change the mean and standard deviation
191 appreciably, although some functions fit the data better than others (see **Materials and**
192 **Methods**, **Figure 2 – figure supplement 2**, and **Table 3**). Furthermore, we inquired whether

193 fluctuations in the instantaneous CW bias, as captured by $p(c)$, could couple to FliM remodeling
194 dynamics and affect the estimates of mean and standard deviation of [CheY-P]. We found that
195 remodeling had no effect on the mean [CheY-P] but led to a small (<25%) increase in the standard
196 deviation (see **Appendix** and **Appendix – figure 1a**), which we ignored in further analysis.

197 As a comparison, we also determined the CW bias distribution $p_{fit}(c)$ and [CheY-P] distribution
198 $p_{fit}(y_P)$ separately for each set of cells with different number of flagella N (**Figure 2b** and **2c**,
199 colored solid curves), along with the best fit distribution of the number of CW flagella, $p_{N,fit}(n_{cw})$
200 (**Figure 2a**, colored solid lines). Although the distributions $p_{N,fit}(n_{cw})$ were better fit for each
201 individual N, the corresponding $p_{fit}(c)$ and $p_{fit}(y_P)$ for each N were comparable to those obtained
202 by a global fit, as shown in **Figure 2b** and **c** (see **Table 4**). The mean and standard deviation in CW
203 bias and in [CheY-P]/K averaged over the separate fits, $\langle\mu_c\rangle = 0.15 \pm 0.03$ and $\langle\sigma_c\rangle = 0.20 \pm 0.02$,
204 $\langle\mu_{y_p}\rangle/K = 0.80 \pm 0.04$ and $\langle\sigma_{y_p}\rangle/K = 0.17 \pm 0.02$, respectively, were almost identical to those
205 obtained by a global fit, indicating that a single global distribution describes the data across N
206 and that the number of flagella does not affect network fluctuations measurably. The above
207 analyses thus show that [CheY-P] fluctuations in free-swimming wild-type cells results in a
208 coefficient of variation $\sigma_{y_p}/\mu_{y_p} = 0.22$.

209 We carried out several tests to confirm that the width of the estimated [CheY-P] distribution
210 resulted from noise in signal transduction. First, we applied our method of analysis to a strain
211 that expresses the constitutively active mutant protein $CheY^{D13K}$, a mimic for CheY-P[24] (strain
212 PM87, henceforth referred to as "CheY*"; see **Materials and Methods**). Since CheY in this strain
213 is decoupled from the upstream network components and the concentration of $CheY^{D13K}$ is
214 determined from gene expression levels, which should not fluctuate on the timescales of our
215 experiments in nutrient-limited conditions[48], we expected to observe smaller fluctuations in
216 [$CheY^{D13K}$] as compared to the wild-type strain. Repeating the above analysis, **Figures 2d-f** show
217 the experimental distributions $p_N(n_{cw})$ along with all fit distributions. Here, the CW bias and FliM
218 dynamics model yielded parameter values $K = 2.5$ μM and $H = 18$, similar to those for wild-type
219 cells, which were used to determine the [$CheY^{D13K}$] distribution. Values for the mean [$CheY^{D13K}$]
220 and standard deviation relative to K from fits for each N and from a global fit are found in **Table**

221 **5**. The mean [CheY-P] relative to K is similar for both strains, and, as expected, fluctuations in the
222 CheY* strain are much reduced compared to the wild-type strain, yielding a coefficient of
223 variation of 0.1.

224 Second, we tested whether the width of the estimated [CheY-P] distribution could be due to
225 cell-to-cell differences in mean [CheY-P] rather than fluctuations arising in signal transduction.
226 To test the contribution of cell-to-cell variation, we determined the best fit [CheY-P] distributions
227 for individual cell traces (**Figure 3 – figure supplement 1** and **figure supplement 2**) and compared
228 the wild-type and CheY* strains. As shown in **Figure 3a** and **3b**, while the mean [CheY-P] relative
229 to K, μ_{y_p}/K, from individual cell distributions was similar for both strains, the coefficient of
230 variation, σ_{y_p}/μ_{y_p}, was significantly smaller for the CheY* strain as compared to the wild-type
231 strain ($p \sim 10^{-4}$), as expected. Importantly, the coefficient of variation for individual wild-type cells
232 averaged over N, $\langle\sigma_{y_p}/\mu_{y_p}\rangle \approx 0.24$, was close to that determined over the population. This
233 indicates that cell-to-cell variation over the wild-type cell population does not contribute greatly
234 to the observed width in the [CheY-P] distribution. In contrast, $\langle\sigma_{y^*}/\mu_{y^*}\rangle$ was significantly smaller
235 for individual cells of the CheY* strain, ~0.05, as compared to the population, 0.1. We suspect
236 cell-to-cell $CheY^{D13K}$ expression differences may contribute to the estimated distributions in
237 **Figure 2d-f**. Nevertheless, our results show that we can attribute the width in the [CheY-P]
238 distribution for wild-type cells to fluctuations in [CheY-P] due to signaling activity. Our estimate
239 of CheY-P fluctuations in wild-type cells is consistent with a theoretically predicted lower bound
240 of 20% of the mean[49].

241 Our method for determining [CheY-P] fluctuations in terms of the functional [CheY-P]
242 concentration allows us to make one interesting observation. Comparing our estimated
243 distribution to the Hill curve relating CW bias to [CheY-P], Eq. (3) (**Figure 2c**), we notice that the
244 peak of the distribution resides at low CW biases, $c < 0.05$, corresponding to CCW flagellar
245 rotation and running a majority of the time. CW rotation and tumbling thus result from
246 fluctuations away from the peak, in the tail of the distribution at higher [CheY-P]. This finding
247 contrasts with the conventional view that the network is poised near the midpoint of the Hill
248 curve[25,36], i.e. with $p(y_P)$ sharply peaked near [CheY-P] ≈ K, and suggests that fluctuations are a
249 critical determinant of the tumbling frequency.

250

251 **[CheY-P] fluctuations decrease upon stimulating the network to increase CW bias**

252 Having characterized fluctuations in the chemotactic network in the steady state, we next
253 investigated them in a network stimulated by a perturbation. In response to a stepwise change
254 in chemical environment, the intracellular [CheY-P] changes rapidly, and then reverts to its
255 steady-state value through adaptation[50–52]. Applying a large stepwise decrease in attractant leads
256 to a transient increase in [CheY-P] and flagellar motor CW bias followed by a decrease to the
257 steady state[42,53], allowing us to measure network fluctuations across the sensitive range of the
258 motor CW bias vs. [CheY-P] curve, Eq. (3).

259 We measured the response of individual cells to a decrease in concentration of α-methyl-DL-
260 aspartate (MeAsp), a non-metabolizable analog of L-aspartate[54] that acts as a
261 chemoattractant[54,55]. We used a three-channel flow chamber (**Figure 4a**) to observe the effect of
262 a step-down from 1 to 0 mM MeAsp on individual optically trapped wild-type cells. The step-
263 down was applied by quickly moving a trapped cell from the middle channel of the flow chamber
264 containing 1 mM MeAsp (**Figure 4a**; labeled "blank + attractant") to the top channel containing
265 no MeAsp (labeled "blank"; see **Materials and Methods**). The run-tumble behavior of the cell
266 was monitored pre- and post-stimulus via the optical traps (see **Materials and Methods**),
267 whereas the flagellar rotation state was measured by fluorescence imaging only post-stimulus.

268 **Figure 4b** shows a representative measurement of a cell with 3 flagella undergoing a step-
269 down stimulus at t = 0. In response, the cell exhibits the expected increase in tumbling
270 immediately post-stimulus, followed by relaxation to the pre-stimulus steady state as the cell
271 adapts (**Figure 4 – figure supplement 1**). As the probability of tumbling is directly related to the
272 probability of CW flagellar rotation[39], n_{cw} measured by fluorescence imaging post-stimulus also
273 relaxes to lower values as the cell adapts (**Figure 4b**, blue trace). Since the [CheY-P] distribution
274 is time-dependent in cells responding to a step-down, the time traces of n_{cw} for each cell were
275 divided into time windows corresponding to 20% of the cell's adaptation time (**Figure 4c**, colors
276 corresponding to time window), over which the average tumble bias was constant to within ~10-
277 20%. The best fit [CheY-P] distribution $p_{fit}(y_P)$ was estimated separately for each window (see
278 **Materials and Methods** for more details on windowing). All data from cells with the same total

279 number of flagella (in **Figure 4c**, three representative cells with N = 3 flagella) were pooled in
280 similarly constructed time windows and used to create histograms $p_N(n_{cw})$ at each time (**Figure**
281 **4d**). $p_{fit}(y_P)$ corresponding to each time window was then found as described above (**Figure 4e**,
282 colored curves). Relative to unstimulated cells (**Figure 4e**, gray curve for unstimulated wild-type
283 cells with N = 3 flagella), the peak of the [CheY-P] distribution shifted to a higher value
284 immediately after the stimulus, as expected for a step down. While we expected the standard
285 deviation to increase as the mean [CheY-P] increased, the width of the [CheY-P] distribution
286 instead decreased (**Figure 4e**). We verified that the reduction in noise was due to a change in
287 chemotaxis network dynamics after stimulation rather than due to windowing of the data; the
288 [CheY-P] distribution widths in adapting cells compared to those in steady-state cells over
289 similarly sized 3-s time windows were significantly different (p = 0.05).

290 The time-dependent, post-stimulus mean relative to the unstimulated global mean $\mu_{y_p}/\mu^0_{y_p,\mathrm{glo}}$
291 and coefficient of variation σ_{y_p}/μ_{y_p} of [CheY-P] for cells with N = 2, 3, 4 flagella are shown in **Figure**
292 **5a** and **5b** (colored filled circles), respectively. The corresponding normalized steady-state mean
293 and coefficient of variation obtained from **Figure 2** are also plotted for reference (for t < 0,
294 colored open circles). As expected, the trends are similar for cells with different numbers of
295 flagella. Thus, we estimated these parameters from a fit to a global [CheY-P] distribution across
296 cells with different N for each time window (**Figure 5a** and **5b**; gray filled circles; see **Materials**
297 **and Methods**). Consistent with the distributions in **Figure 4d**, the mean [CheY-P] increases
298 immediately in response to the step-down stimulus and relaxes toward its steady-state, pre-
299 stimulus value as the cells adapt. At the same time, the coefficient of variation in [CheY-P] falls
300 post-stimulus, then gradually increases toward the pre-stimulus value.

301 These results point to two interesting features. First, the mean [CheY-P] shows a 20% increase
302 compared to the pre-stimulus steady state immediately after the step down (**Figure 5a**). While
303 the increase in [CheY-P] and the resulting increase in CW bias is expected for a step-down
304 stimulus, it is smaller in magnitude than predicted by existing models[44,56]. Given the strength of
305 the stimulus (from 1 to 0 mM [MeAsp]), these models predict a CW bias close to 1, corresponding
306 to at least a 75% increase in mean [CheY-P]immediately post stimulus; instead, [CheY-P] remains

near the midpoint of the CW bias vs. [CheY-P] curve, $\mu_{y_p} \approx K$ in Eq. (3). Second, fluctuations are significantly reduced immediately after the stimulus is applied, decreasing from $\sigma_{y_p}/\mu_{y_p} = 0.2$ pre-stimulus to as low as $\sigma_{y_p}/\mu_{y_p} = 0.02$ post-stimulus (**Figure 5b**). This value is as low as that measured in individual CheY* cells (**Figure 3b**), suggesting that fluctuations in the network are largely suppressed when driven to high CW bias.

In the above analysis, we assumed the same values for K and H as for steady-state cells (2.4 μM and 18, respectively). However, we expect FliM remodeling to occur in response to the stimulus, leading to a gradual shift in the motor c vs y_P response curve post-stimulus. To determine the size of this effect on the estimates of μ_{y_p} and σ_{y_p}/μ_{y_p}, we carried out simulations of motor remodeling based on the model by Zhang et al.[43] (see **Materials and Methods**). As shown in **Appendix – figure 1**, the estimated μ_{y_p} increases slightly as a consequence of the reported adaptive effect of remodeling[45]. Nevertheless, the qualitative trend of μ_{y_p} vs. time post-stimulus remains. In contrast, σ_{y_p}/μ_{y_p} exhibits only a moderate increase (<15%) when accounting for motor remodeling (**Appendix – figure 1**).

A stochastic model incorporating CheA activity fluctuations reproduces the experimental results

We next sought a stochastic model to describe our experimental results. The intracellular CheY-P is controlled by fast phosphorylation-dephosphorylation reactions,

$$\text{CheY} \underset{k_z}{\overset{k_A a}{\rightleftharpoons}} \text{CheY-P}\,, \tag{6}$$

in which the rate of CheY phosphorylation by the CheA-receptor complex is written as $k_A a$, where a is the probability that CheA is in its active state and k_A is the maximum phosphorylation rate[57,58], and in which k_Z is the rate of CheY-P dephosphorylation by the phosphatase CheZ. These rates are expected to be on the order of 10 s^{-1} [56–58]. We first examined if this set of reactions alone could generate the number fluctuations in CheY-P to reproduce the observed noise. Using the chemical master equation (CME), the following analytical solution for the coefficient of variation in [CheY-P] (see **Materials and Methods**) is obtained[59]:

$$\frac{\sigma_{y_p}}{\mu_{y_p}} = \sqrt{\frac{1}{\mu_{y_p} V_C}\left(1 - \frac{\mu_{y_p}}{y_{tot}}\right)}, \tag{7}$$

where the mean [CheY-P] is given by $\mu_{y_p} = y_{tot} k_A a / (k_A a + k_Z)$ and V_C is the *E. coli* cell volume, assumed to be 1.4 fL[60] ($V_C^{-1} \approx 1.2$ nM).

To compare this model to the experimental data, we plotted in **Figure 5c** the coefficient of variation vs. the mean [CheY-P] for cells at steady state (open circles) and for stimulated cells (filled circles). All of the experimental data fall on one continuous curve. (The same pattern is observed when accounting for motor remodeling on the estimates of μ_{y_p} and σ_{y_p}/μ_{y_p}; **Appendix – figure 1d**). The curve traced out by the data differs from the model Eq. (7) in two significant ways. First, for low mean [CheY-P], Eq. (7) (dotted line in **Figure 5c**) predicts a coefficient of variation σ_{y_p}/μ_{y_p} an order of magnitude smaller than our experimentally determined value. Fundamentally, the low number fluctuations predicted from Eq. (7) are due to the large total number (~8,000) of CheY molecules in the cell. Matching our experimental data would require decreasing the number of CheY by over two orders of magnitude (equivalent to replacing V_C with a cell volume two orders of magnitude smaller in Eq. (7)). Although a recent study proposed that CheY sequestration at the cell poles where many signaling proteins reside may limit the number of CheY-P participating in signaling[61], such a mechanism is unlikely to account for this discrepancy between Eq. (7) and our data.

Second, the dramatic decrease in coefficient of variation near $\mu_{y_p}/\mu^0_{y_p,\mathrm{glo}} \approx 1.2$, which results from the observed narrowing of the [CheY-P] distributions in stimulated cells (**Figure 4e**), is not recapitulated in the model. Eq. (7) predicts a drop to zero at $\mu_{y_p} \approx 10$ μM or $\mu_{y_p}/\mu^0_{y_p,\mathrm{glo}} \approx 5$, when all of the CheY becomes phosphorylated. One possibility to account for these observations is a ceiling of on the amount of CheY available for phosphorylation, leading to a maximum relative [CheY-P] ≈ 1.2 and a reduction in the width of the [CheY-P] distribution at this concentration. To test this mechanism, we constructed a mutant *ΔcheZ* strain ("RB03"; see **Materials and Methods**) lacking the phosphatase CheZ, in which all the available CheY is expected to be phosphorylated. We replicated our flagellar imaging analysis and calculated the [CheY-P] distribution for this strain, assuming the same values for *K* and *H* as for wild type cells (2.4 μM and 18, respectively).

361 This yielded a mean [CheY-P]/K of 1.6 ± 0.1, corresponding to a CW bias close to 1 according to
362 Eq. (3) (data not shown), higher than that observed following a step-down stimulus, ruling out
363 such a mechanism. This result holds when we account for the effect of motor remodeling in this
364 strain, which manifests as an increase in K compared to the wild type strain, since the mean
365 [CheY-P] scales with K.

366 An alternate, more plausible mechanism is that additional sources of noise contribute to the
367 two-species model in Eq. (6). One such source is fluctuations in phosphorylation-
368 dephosphorylation kinetics. Although Eq. (6) assumes constant rates, the activity of the CheA-
369 receptor complex is thought to fluctuate over time[31,32]. To model CheA fluctuations, we modified
370 Eq. (6) to allow CheA to interconvert between active and inactive states, leading to a fluctuating
371 activity $a(t)$. Adapting the approach of Paulsson et al.[62,63], the following analytical solution for the
372 coefficient of variation in [CheY-P] in the presence of CheA fluctuations is obtained (see **Materials**
373 **and Methods**):

374 $$\frac{\sigma_{y_P}}{\mu_{y_P}} = \sqrt{\frac{1}{\mu_{y_P} V_C}\left(1-\frac{\mu_{y_P}}{y_{tot}}\right)\left[1+\langle b\rangle\left(1-\frac{\mu_{y_P}}{\alpha y_{tot}}\right)\right]}, \quad (8)$$

375 where the factor in brackets represents the contribution of CheA activity fluctuations to CheY-P
376 noise. Here $\langle b\rangle$ denotes the number of new CheY-P generated during the time periods when
377 CheA is active. The factor $\alpha \equiv k_A/(k_A+k_Z)$ is the fraction of CheY that is phosphorylated when all
378 CheA are active, i.e. when the activity a = 1.

379 This model recapitulates the features of the data well; **Figure 5c** shows a fit to Eq. (8) (dashed
380 line) with parameters $\langle b\rangle$ = 280 ± 80 and α = 0.240 ± 0.003 (R^2 = 0.6; errors represent 95%
381 confidence interval). (Fits of the data in **Appendix – figure 1**, which account for motor remodeling
382 yield an almost identical value of α and a ~70% higher $\langle b\rangle$). Analogous to "burst size" in
383 stochastic gene expression[64,65], $\langle b\rangle$ increases number fluctuations in CheY-P, matching the data.
384 The parameter α represents the fact that the contribution of CheA fluctuations to CheY-P noise
385 must go to zero (as in in **Figure 5c**) when a = 1, at a mean [CheY-P] of $\mu_{y_P} = \alpha y_{tot}$ ≈ 2 μM. The value
386 of α points to a kinetic ceiling on CheA-receptor complexes of $k_A = 0.32k_Z$, or ~10 s^{-1} assuming a

387 constant CheY-P dephosphorylation rate of $k_Z = 30\ s^{-1}$, within the reported range[56–58]. A maximum
388 rate $k_A = 10\ s^{-1}$ is consistent with reported values of the CheA auto-phosphorylation rate, the rate-
389 limiting step for CheY phosphorylation[35,56–58]. (We note that in the *ΔcheZ* strain, the kinetic ceiling
390 on k_A would not cap [CheY-P] since $k_Z = 0$.)
391

392 ## Discussion

393 In this work we demonstrate a new approach for inferring fluctuations in [CheY-P] based on
394 the statistics of flagellar switching in multi-flagellated *E. coli* cells. One advantage of this approach
395 is that its accuracy in quantifying network noise does not depend on temporal averaging, which
396 limited previous measurements to long time scales (>10 s)[31,33], but instead relies on multiple
397 flagellar motors making independent simultaneous "measurements" of intracellular CheY-P
398 levels. This feature allows us to measure [CheY-P] noise at short timescales (0.5-5 s) and to track
399 the time evolution of signaling noise in cells as they undergo adaptation.

400 Another advantage of this method is that noise parameters are determined in terms of CheY-
401 P concentration (relative to K), which allows for direct comparison to theoretical models. In
402 contrast, prior fluorescence-based studies determine changes in CheA activity relative to a
403 baseline[32,33]. However, one limit is that our estimate of $p(y_P)$ depends on the relation between
404 CW bias and [CheY-P], parametrized by K and H in the Hill curve, Eq. (3). As discussed above, we
405 consider uncertainties and variations in these parameters in our analysis. It is important to
406 highlight that the relative differences between various [CheY-P] distributions—such as between
407 different time points in adapting cells—still remain significant (see **Appendix – figure 1**). Thus,
408 the trends in our results remain valid independent of parameter values.

409 Previous single-cell measurements of flagellar rotation by bead tracking[31,41] and of CheA
410 activity using fluorescent reporters[32,33] have reported long-term noise in the chemotaxis network
411 attributed to CheR-CheB methylation-demethylation dynamics[31] and, recently, new sources such
412 as receptor clustering and other dynamics[32,33]. A direct comparison between these results and
413 ours is difficult because of the differences in timescales between the measurements (0.1-40 s vs.
414 10-1000 s). While our approach extends to fast timescales, photobleaching of the dyes limits the
415 duration of our traces and limits the overlap between the measurement timescales.

416 Nevertheless, to attempt such a comparison, we determined how our estimate of CheY-P noise
417 varies with the measurement time window. As shown in **Figure 5 – figure supplement 1**, the
418 noise increases with longer windows. This trend is consistent with our short-time measurements
419 capturing the tail of a longer-timescale noise source. We are unable to determine the timescale
420 precisely, but estimate that it must be >10 s, consistent with reported values of ~13 s[32,33]. Thus,
421 it is plausible that these different measurements are consistent and that source of CheY-P noise
422 are the same. Nevertheless, we have deliberately made our model for CheA activity fluctuations
423 in Eq. (8) agnostic to the source of noise to allow for alternatives.

424 The noise characteristics of the chemotaxis network revealed in our measurements may have
425 functional consequences. Our findings suggest that [CheY-P] fluctuations are critical drivers for
426 CW flagellar rotation/tumbling in *E. coli*. Our experimentally determined mean [CheY-P]/K of 0.8
427 restricts the cell to a CW bias <0.05, corresponding to running the majority of the time.
428 Previously, Terasawa et al.[38] proposed that waves of CheA activity could cause transient increases
429 in [CheY-P]. Our data and model appear to be consistent with this mechanism, with the "burst
430 size" $\langle b \rangle$ in Eq. (8) representing such waves in activity. Our fit parameters indicate that ~3.5% of
431 all CheY are phosphorylated during such events. We envision that transient increases in [CheY-
432 P], driven by waves of phosphorylation by the receptor kinase complex[38], increases the CW bias
433 to generate tumbles. In previous work, it was proposed that [CheY-P] fluctuations act to
434 synchronize flagellar switching[38,39], which was shown to make swimming behavior robust to
435 variation in flagella number[39]. *E. coli* has also been proposed to exploit long-timescale [CheY-P]
436 fluctuations to explore larger volumes of space[31,34] and to increase drift speeds, enhancing
437 migration along increasing attractant gradients[35–37]. Lastly, the kinetic ceiling in receptor kinase
438 activity which restricts CheY-P fluctuations when the mean [CheY-P] increases could prevent
439 CheY-P concentrations from saturating and leading to continuous and unproductive CW flagellar
440 rotation/tumbling. Such behavior could result in increased *E. coli* swimming efficiency down
441 steep decreases in attractant concentration, as likely found in natural environments.
442

443 **Acknowledgements**

444 We are thankful to Tom Kuhlman for guiding us through the process of molecular cloning, and to
445 Howard Berg for providing bacterial strains. We thank members of the Chemla laboratory for
446 scientific discussions and Christopher Rao for providing comments on the manuscript. Work in
447 the Chemla and Golding labs is supported by National Science Foundation Physics Frontiers
448 Center (PFC) "Center for the Physics of Living Cells" (CPLC) PHY-1430124. Work in the Golding lab
449 is supported by the National Institutes of Health grant no. R01 GM082837.

450 ## Materials and Methods

451 ### Microbiology

452 **Cell preparation**

453 Experiments were performed on the HCB1660 *E. coli* strain, a gift from the Berg lab[66]. This strain
454 is considered wild-type for chemotaxis but is *ΔfliC* expressing $FliC^{S219C}$ under the control of the
455 P_{araBAD} promoter. The mutant $FliC^{S219C}$ protein was specifically labelled with a cysteine reactive
456 fluorescent dye, Alexa Fluor 532 C_5 Maleimide (A10255, ThermoFisher Scientific) using the
457 method first described by Turner et al.[66] and later used by Mears et al.[39]. The strain referred to
458 as CheY* is PM87, *ΔfliC ΔcheBYZ* expressing $FliC^{S219C}$ and constitutively active $CheY^{D13K}$,
459 constructed by Mears et al.[39]. The strain referred to as RB03 (constructed for this work) is *ΔfliC*
460 *ΔcheZ* expressing $FliC^{S219C}$.

461 As described by Mears et al.[39], for each experiment, a single colony from an LB, lysogeny
462 broth, agar plate was inoculated into 1 mL tryptone broth (TB: 0.8% [wt/vol] NaCl, 1% Bacto
463 Tryptone), and grown to saturation overnight (14-18 hours), shaking at 265 RPM at 30°C with the
464 appropriate antibiotics. The overnight culture was diluted 100-fold into 12 mL TB, and grown to
465 OD_{600} ~0.4 to 0.5, with 0.01% [wt/vol] or 666 µM L-arabinose, shaking at 265 RPM at 30°C for
466 ~4.5 hours. The over-day culture was washed twice by slow centrifugation (1300 × *g*) and gently
467 resuspended in 1 mL motility buffer (MB: 10 mM Phosphate Buffer [pH 7.0], 70 mM NaCl and 0.1
468 mM EDTA)[21].

469 To label flagella fluorescently, we followed the protocol reported by Mears et al.[39]. An
470 appropriate volume of the Alexa Fluor 532 C_5 Maleimide dye was added to resuspended cells in
471 0.5 mL MB to a concentration of ~0.01 mg/mL and incubated with slow rotation (~10 RPM) at
472 room temperature in the dark for 90 min. The labeled cells were gently resuspended in 1 mL MB.
473 For trapping, cells were diluted 20-fold in trap motility buffer (TMB: 70 mM NaCl, 100 mM Tris-
474 Cl, 2% [wt/vol] glucose, with 0.1 mM methionine and an oxygen-scavenging system [290 µg ml^{-1}
475 pyranose oxidase and 65 µg ml^{-1} catalase][40]) and injected into the flow chamber for the trapping
476 experiment. When handling resuspended cells, at all times, we avoided pipetting, or we used
477 wide orifice pipette tips to avoid shearing flagella.

478 1 mg of the dry Alexa Fluor 532 C_5 Maleimide dye was dissolved in 250 µL water by vortexing
479 and stored in aliquots at -20°C. The stock concentration for each aliquot was determined using
480 UV-Visible Absorption Spectroscopy. Since this dye does not dissolve readily in water, we found
481 it important to determine the concentration for each aliquot separately for optimal labeling.
482
483 **Construction of strains**
484 The bacterial strains and plasmids used for this work are listed in **Table 1**. Oligonucleotides for
485 generating mutations and creating plasmids are listed in **Table 2.** All primers were purchased
486 from Integrated DNA Technologies (Coralville, Iowa). The *CheZ* chromosomal deletion was carried
487 out using the standard λ Red recombinase system developed by Datsenko and Wanner[67]. The
488 strain referred to as RB03 was created from HCB1613 (AW405, chemotaxis wild-type with a
489 functional FliC deletion). To create the strain RB01, *CheZ* was replaced by a chloramphenicol
490 resistance cassette with flanking FRT (Flp recombinase-recombination target) sites using the
491 primers CheZ-pKDF and CheZ-pKDR with pKD3 as a template. This replacement was accomplished
492 via the λ Red recombinase enzymes expressed from pKD46. The chloramphenicol cassette was
493 eliminated via Flp recombinase expressed from pCP20 to obtain strain RB02. Finally, the strain
494 RB03 was created by transforming strain RB02 with the plasmid pBAD33 that expresses $FliC^{S219C}$.
495 Standard molecular cloning techniques were used to purify plasmids and perform PCRs.
496

497 ## Data Acquisition

498 **Optical trapping of individual *E. coli* with simultaneous fluorescence imaging**
499 Experiments were performed with a dual-trap optical tweezers instrument combined with epi-
500 fluorescence slim-field imaging, developed and described in detail in previous work by Mears et
501 al.[39]. Briefly, the optical traps were created from a single 5-W, 1064-nm laser (YLR-5-1064-LP, IPG
502 Photonics). Two trapping beams were generated by timesharing, intermittently deflecting the
503 input beam between two positions with an Acousto-Optic Deflector, AOD (DTSXY-250-1064, AA
504 Opto-Electronic). The two resulting beams were then tightly focused using a 60X, water
505 immersion (1.2 NA) objective (Nikon, Tokyo, Japan) to create two optical traps. An identical
506 objective was used to collect the transmitted trap light for position detection and for bright-field

507 imaging of the cells using Koehler illumination from a blue LED. A bacterial cell could be captured
508 and aligned between the two optical traps without impeding its rotatory motion. The light
509 scattered by the trapped cell was collected onto a position sensitive photodetector and used to
510 monitor cell motion, which was analyzed to determine runs and tumbles as described below and
511 previously by Min et al.[40].

512 Fluorescently labeled flagella of trapped cells were imaged using a 532-nm laser (TECGL-30,
513 World Star Tech) aligned for slim-field illumination[68], with the excitation beam diameter at the
514 sample plane ~10-15 µm. We strobed the fluorescence excitation and trap laser illumination out
515 of phase with each other to minimize photobleaching[39]. The fluorescence illumination was
516 strobed by using an Acousto-Optic Modulator, AOM (802AF1, IntraAction) to deflect the
517 excitation light intermittently into the sample plane for a duration of 16-20 µs each cycle while
518 the traps were off. An EMCCD camera (iXon3 860 EMCCD, Andor) recorded images in synchrony
519 with the excitation pulse at the rate of 100 frames per second to capture focused images of the
520 flagella as they rotated at a rate of ~100 Hz. In this manner, movies of flagellar motion were
521 recorded, typically for ~30-40 s until the flagella photobleached. Movies were saved using the
522 Solis software (Andor) and processed using custom written code in MATLAB. Each movie was
523 analyzed manually to count flagella and their transitions between CW and CCW rotating states.
524

525 **Motility assays combined with fluorescence imaging in trapped cells**

526 Custom-built microfluidic chambers shown in **Figure 1c** and **4a** (preparation described in detail
527 in Mears et al.[39] and Min et al.[42]) were used to perform motility assays coupled with fluorescence
528 imaging of labeled flagella on individual trapped cells. To prepare chambers, glass coverslips were
529 sonicated in acetone, then rinsed in deionized water. This step was followed by rinsing in
530 methanol and drying under nitrogen flow. The flow channels in the chamber were cut out from
531 Nescofilm (Alfresa Pharma Corporation, Osaka, Japan) and bonded to glass coverslips as
532 described previously[39,42].

533 For measurements of free-swimming, or unstimulated, cells, the chamber contained two
534 channels (**Figure 1c**). The upper channel contained trap motility buffer (TMB) only, while the
535 lower channel contained *E. coli* cells in TMB. Both channels were continuously injected with the

536 appropriate solutions using a syringe pump (PHD2000, Harvard Apparatus) with a linear flow rate
537 of ~30 µm/s. Cells were trapped in the lower channel and moved to the upper channel by
538 displacing the chamber with respect to the traps using a motorized three-axis translational stage
539 (ESP301; Newport, Irvine, California). Once the trapped cell was aligned between the two traps
540 in the upper channel, the bright-field illumination was turned off and the 532-nm excitation
541 illumination was turned on. Cell motion was observed by simultaneously recording the optical
542 trap signal sensed by position sensitive photodetectors and the fluorescence signal from labelled
543 flagella sensed by the EMCCD camera.

544 For measurements of stimulated cells undergoing chemotactic adaptation, the chamber
545 contained three channels (**Figure 4a**). For a step-down stimulus, the top ("blank") channel
546 contained TMB only, the middle ("blank + attractant") channel contained TMB, 1 mM *α*-methyl-
547 DL-aspartate (MeAsp) and Rhodamine B (100 nM), and the bottom ("cell + attractant") channel
548 contained TMB, 1 mM MeAsp and *E. coli* cells. Fluorescence imaging of the Rhodamine B diffusion
549 profile was used to characterize the gradient formed across the top and the middle channel, as
550 described by Min et al.[42]. All three channels of the flow chamber were injected with their
551 solutions at a linear flow rate of ~50 µm/s. In a typical experiment, a swimming cell was first
552 captured from the "cells + attractant" channel. The trapped cell was moved to the "blank +
553 attractant" channel, aligned between the two traps, and oriented along the direction of the flow.
554 Pre-stimulus optical trap signal of the swimming cell was recorded for ~200 s (without any
555 fluorescence imaging of flagella). The trapped cell was then moved at the speed 100 µm/s to the
556 "blank" channel so that it experienced a step down in MeAsp concentration over a ~4-s duration
557 (as shown in Figure S1 in Min et al.[42]). During this move, the bright field illumination was turned
558 off and the 532-nm excitation illumination was turned on. The chemotactic response of the
559 captured cell was recorded in the "blank" channel by simultaneously recording the optical trap
560 signal and the fluorescence signal from labelled flagella. While the trap signal post-stimulus was
561 recorded for ~400 s, the EMCCD signal was recorded only for ~30-40 s until the flagella
562 photobleached.

563

564 Raw Data Analysis

565 **Run-tumble analysis for optical trap data**

566 Cell motion was detected from imaging the optical trap light scattered by the cell body onto
567 position-sensitive photodetectors, as described previously by Min et al.[40]. This optical trap signal
568 was analyzed for runs and tumbles. Briefly, runs corresponded to oscillatory signals due to cell
569 body roll at a frequency ~10 Hz, while tumbles corresponded to erratic trap signals with a
570 frequency <1 Hz. We used custom-written MATLAB code incorporating a wavelet analysis to
571 identify the peak body roll frequency at every time point of each data trace and to assign runs
572 and tumbles by specifying an appropriate frequency threshold[40]. An example trace of the trap
573 signal and the corresponding run-tumble assignment is shown in **Figure 1c** and **d** in earlier work
574 by Mears et al.[39].

575

576 **Image analysis for fluorescence data**

577 Images acquired using the high-speed fluorescence imaging described above were adjusted for
578 contrast to best visualize the flagella. Each movie was played in slow motion and Clockwise
579 (CW)/Counter Clockwise (CCW) states were assigned manually to each flagellum over a time
580 window of 100 ms (i.e. 10 frames). As described previously[21,39], the CCW/CW rotation state of
581 the flagella can be visually identified from their different helical waveforms, commonly referred
582 to as 'normal', 'semi-coiled', 'curly-1' and 'curly-2'. CCW-rotating flagella exclusively adopt the
583 'normal' waveform and CW-rotating flagella adopt the 'semi-coiled' and 'curly-1' waveforms the
584 majority of the time. Waveform transitions take less than ~0.5 s to propagate through the
585 flagella.

586

587 ## Modeling and Analysis

588 **Extracting [CheY-P] distributions from flagellar rotation data**

589 In flagellar imaging movies of individual cells, we tracked the CW/CCW state of each flagellum—
590 hence the number of CW flagella in time—and determined $p_N(n_{cw})$, the probability that n_{cw} out
591 of a total of N flagella rotate CW, where $n_{cw} = 0, 1 \ldots N$. From first principles[69], we can relate $p_N(n_{cw})$
592 to the instantaneous CW bias of the motor, c through Eq. (1), where $p(c)$ is the distribution in

motor bias c, the probability that a motor rotates CW. The motor bias takes values between 0 and 1. $p_N(n_{cw}|c)$, the conditional probability that n_{cw} out of N flagella are CW given a certain bias c, is given by the binomial distribution in Eq. (2), since as shown in previous work by Mears et al.[39], the flagellar motors switch independently.

We can thus use Eq. (1) and (2) to estimate the motor bias distribution $p(c)$ from measurements of $p_N(n_{cw})$. In general, this integral equation cannot be solved by a unique solution $p(c)$; instead, $p(c)$ becomes more tightly determined as the number of flagella N increases. This can be seen by noting that $p_N(n_{cw}|c)$ in Eq. (2) is a polynomial in c of order N. Therefore, the integral Eq. (1) for $p_N(n_{cw})$ yields a sum over the first N moments of the distribution $p(c)$,

$$\begin{aligned} p_N(n_{cw}) &= \sum_{r=n_{cw}}^{N} \frac{N!}{n_{cw}!(r-n_{cw})!(N-r)!}(-1)^{r-n_{cw}} \int_0^1 c^r p(c)dc \\ &= A^{(N)}_{n_{cw},n_{cw}} \left\langle c^n \right\rangle + A^{(N)}_{n_{cw},n_{cw}+1} \left\langle c^{n+1} \right\rangle + \cdots A^{(N)}_{n_{cw},N} \left\langle c^N \right\rangle = \sum_{r=0}^{N} A^{(N)}_{n_{cw},r} \left\langle c^r \right\rangle \end{aligned} \tag{9}$$

where each moment is given by $\left\langle c^r \right\rangle = \int_0^1 dc\, c^r p(c)$ and the (N+1) × (N+1) upper triangular matrix $A^{(N)}_{n_{cw},r}$ is defined in the second line. This matrix equation can be inverted to give $\left\langle c^r \right\rangle$ in terms of a sum of $p_N(n_{cw})$ over n_{cw}. For a cell with N flagellar motors, inversion of Eq. (9) yields only the first N moments of the distribution $p(c)$, $\left\langle c \right\rangle$, $\left\langle c^2 \right\rangle$, … $\left\langle c^N \right\rangle$. Short of knowing every moment, the distribution $p(c)$ can only be approximated using the finite number of moments. Nevertheless, the first two moments are generally sufficient to assess the overall shape of the distribution, which is adequate for our purposes, and we analyze cells with $N \geq 2$.

An alternate formulation is to express the integral equation in terms of the concentration of phosphorylated CheY, [CheY-P] is Eq. (4) where y_P is the cellular [CheY-P] and $p(y_P)$ is the distribution of [CheY-P]. y_P can take values between 0 to y_{tot}, the total cellular [CheY]. The conditional probability $p_N(n_{cw}|y_P)$ can be obtained from $p_N(n_{cw}|c)$ in Eq. (2) by making use of the relation between the motor bias c and y_P determined by Cluzel et al., Eq. (3) [25]. The conditional probability $p_N(n_{cw}|y_P)$ is obtained by combining Eq. (2) and Eq. (3) to yield Eq. (5). We can transform between $p(c)$ and $p(y_P)$ using the following relationship:

$$p(y_P) = p(c)\frac{dc}{dy_P},$$

which, using Eq. (3) gives

$$p(y_P) = p(c)\frac{HK^H y_P^{H-1}}{\left(K^H + y_P^H\right)^2}. \tag{10}$$

Local and global fitting with trial distributions and error analysis

Since the form of the distribution $p_N(n_{cw})$ depends on the number of flagella, we constructed separate distributions for cells with different numbers of flagella *N*, as shown in **Figure 2a** and **d**. [CheY-P] distributions were estimated for each data set by assuming a trial distribution function p_{fit} (of either motor bias, *c*, or [CheY-P], y_P) with a small number of shape parameters (two), evaluating $p_{N,fit}(n_{cw})$ using the integral in Eq. (1) or (4), and finding the shape parameters that best fit the experimentally observed distribution $p_{N,obs}(n_{cw})$. Without a priori knowledge of the appropriate form for the trial distribution function p_{fit}, we tested three different functions. One was a beta distribution in *c*,

$$p_{fit}(c) = \frac{(1-c)^{\beta-1}c^{\alpha-1}}{B(\alpha,\beta)}, \tag{11}$$

where $B(\alpha,\beta) = \int_0^1 (1-x)^{\beta-1}x^{\alpha-1}dx$ is the beta function and the shape parameters $\alpha,\beta > 0$. The beta distribution was chosen because it is defined over the range 0 to 1, the same as for the motor bias *c*. α and β were the fitting parameters and used to determine the mean and variance of the motor bias, $\langle c\rangle = \frac{\alpha}{\alpha+\beta}$ and $\langle c^2\rangle - \langle c\rangle^2 = \frac{\alpha\beta}{(\alpha+\beta)^2(\alpha+\beta+1)}$, respectively. To determine the corresponding mean, μ_{y_P}, and standard deviation, σ_{y_P}, of the [CheY-P] distribution, we first calculated the probability density function $p(y_P)$ from $p(c)$ according to Eq. (10) and then evaluated the mean and standard deviation numerically from their definitions.

For comparison, we also tested Gaussian and gamma trial distributions for $p_{fit}(y_P)$, using the alternate formulation described in Eq. (4). For the Gaussian distribution,

$$p_{fit}(y_P) = \frac{1}{\sqrt{2\pi\sigma_{y_P}^2}} \exp - \frac{(y_P - \mu_{y_P})^2}{2\sigma_{y_P}^2}. \quad (12)$$

The fitting parameters were the mean and standard deviation, μ_{y_P} and σ_{y_P}. For the gamma distribution,

$$p_{fit}(y_P) = \frac{1}{\Gamma(k)\theta^k} y_P^{k-1} \theta^{-\frac{y_P}{\theta}}, \quad (13)$$

the fitting parameters were the shape parameters k and θ, with the mean and the standard deviation in [CheY-P] corresponding to $\mu_{y_P} = k\theta$ and $\sigma_{y_P} = \sqrt{k\theta^2}$, respectively.

We found the shape parameters that best fit the experimentally observed distribution $p_{N,obs}(n_{cw})$ using a χ^2 minimization routine, where the figure of merit χ_N^2 was defined as:

$$\chi_N^2 = \sum_{n=0}^{N} \frac{N_{data}(p_{N,fit}(n_{cw}) - p_{N,obs}(n_{cw}))^2}{p_{N,fit}(n_{cw})}, \quad (14)$$

where N_{data} is the number points used to construct each distribution $p_{N,obs}(n_{cw})$. We report the reduced χ^2 in **Table 3**, calculated by dividing χ_N^2 in Eq. (14) by the degrees of freedom, which in our case is the difference between the number of independent data points in each distribution $p_{N,obs}(n_{cw})$ and the number of independent parameters used to determine $p_{N,fit}(n_{cw})$. For example, for cells with N = 3 flagella, the number of independent data points in $p_{N,obs}(n_{cw})$ is 3, and the number of independent fitting parameters used to estimate $p_{N,fit}(n_{cw})$ is 2, hence the degrees of freedom is 1. We note that for N = 2, the degrees of freedom is 0 and thus a reduced χ^2 is undefined. This reflects the fact that cells with two flagella determine exactly two moments of the fitting distribution function, and thus the two shape parameters. For a population of cells with the same number of flagella N, we estimated the error in the calculated [CheY-P] distribution and hence its mean and standard deviation by bootstrapping, where individual cell time traces were resampled with replacement and input into the χ^2 minimization routine.

In addition to calculating [CheY-P] distributions separately for each number of flagella N, we estimated a single global [CheY-P] distribution that fit all datasets across all N. Corresponding to

663 this distribution, we found a single set of parameters that best fit $p_{N,obs}(n_{cw})$ separately for each N

664 by minimizing a combined χ^2

665 $$\chi^2_{global} = \frac{\sum_{N=2}^{5}(N+1)\chi^2_N}{\sum_{N=2}^{5}N+1}, \quad (15)$$

666 where χ^2_N is calculated according to Eq. (14). The reduced χ^2 for this global fitting was calculated

667 as described above, with the degrees of freedom equal to 12 (equal to the total number of

668 independent data points in $p_{N,obs}(n_{cw})$ over all N, 14, minus the number of independent fitting

669 parameters used to estimate $p_{N,fit}(n_{cw})$, 2). To estimate the error in the global [CheY-P]

670 distribution, we applied the global χ^2 minimization routine similar to above, and bootstrap

671 resampled all datasets across all flagellar numbers N (as opposed to resampling over each N

672 separately). We then sorted the resampled data by N for separate analysis using Eq. (1) or (4).

673 Finally, we also calculated CheY-P distributions for each individual cell for each number of

674 flagella N. We estimated the error in the individual cells' CheY-P distributions using bootstrapping

675 as described above. 0.5-s long time windows of individual cell n_{cw} time traces were resampled

676 with replacement to construct traces for each bootstrapping trial, and the corresponding

677 $p_{N,obs}(n_{cw})$ was input into the χ^2 minimization routine. A 0.5-s window duration was chosen based

678 on the average autocorrelation time for individual cell n_{cw} time traces, determined to be ~0.3 s

679 across N. Time windows of duration of 0.5 s, about twice as long as the autocorrelation time, are

680 sufficiently long to be uncorrelated and suitable for the purposes of bootstrapping.

681 **Figure 2 – figure supplement 2** compares examples of the three trial distribution functions

682 $p_{fit}(y_P)$ that best fit the same data set, and **Table 3** displays the corresponding best fit values of

683 the mean and standard deviation μ_{y_P} and σ_{y_P} for the three trial functions. All three yielded

684 similarly shaped best fit distributions, and similar values for μ_{y_P} and σ_{y_P}, although the beta- and

685 Gaussian-based trial distributions, Eq. (11) and (12), consistently yielded better fits than the

686 gamma-based distribution Eq. (13) (compare χ^2 in **Table 3**).

687 For the results reported in **Figure 2-5** and their supplements, we used the beta trial function
688 to estimate the [CheY-P] distribution. We also estimated [CheY-P] distributions for the mutant
689 *ΔcheZ* strain lacking the phosphatase CheZ ("RB03), in which all the available CheY is expected to
690 be phosphorylated. We found that the beta distribution trial function was not well-behaved for
691 this extreme case, hence the result reported for this strain is for a Gaussian trial function.
692
693 **Custom statistical test**
694 In order to make comparisons between sets of data points each with an error bar (for example,
695 in **Figure 3**), standard statistical tests such as the t-test and Wilcoxon rank sum test could not be
696 used. Hence a custom statistical test based on the permutation test[70] was written in order to
697 make such comparisons. The null hypothesis for this test was that the observed means of the two
698 data sets are equal. First, surrogate data sets were created under the assumption of this null
699 hypothesis. Surrogate data for each data point in the two data sets being compared was created
700 by random sampling from a gamma distribution with mean equal to the value of the data point
701 and the standard deviation equal to the value of the error bar on the data point. Next, the labels
702 on each point in the surrogate data were randomly permuted to create two separate surrogate
703 data sets with the same number of points as the ones being compared. For each such pair of
704 surrogate data sets, a test statistic under the null hypothesis was calculated as the difference of
705 their means. For 50,000 such surrogate data sets, the probability distribution of the test statistic
706 under the null hypothesis was plotted. The P-value for this custom statistical test was calculated
707 as the probability of finding the value of the test statistic, i.e. difference between means under
708 the null hypothesis, that is greater than the observed difference of means.
709
710 **Estimating [CheY-P] distributions for stimulated cells**
711 The flagellar imaging data for trapped cells experiencing a step-down in MeAsp were also
712 analyzed to record the number of CW flagella with time. Since the motor bias varies with time
713 during adaptation, each individual cell time trace was divided into non-overlapping windows the
714 duration of which was determined from the cell's adaptation time. For each cell, the collected
715 optical trap signal was analyzed for runs and tumbles, and the tumble bias was calculated from

716 the fraction of time the cell tumbled over a 10-s sliding time window. The time trace of the tumble
717 bias was fit to the following expression:

718 $$TB(t) = TB_{\infty} + ae^{-bt} + ce^{-dt} \quad (16)$$

719 where *a, b, c* and *d* are fitting parameters, and TB_{∞} is the tumble bias of the cell when it has
720 adapted to the stimulus. The adaptation time was approximated as $t_{adap} = \ln(2)/b$ following a
721 procedure used by Min et al.[42] An example fit is shown in **Figure 4 – figure supplement 1.**

722 Windows of duration $0.2t_{adap}$ were selected starting at the time of the stimulus, $t = 0$, until t
723 $= 1.6t_{adap}$, where t_{adap} for our dataset was found to be ~3s. A final window of variable length
724 between $0.5t_{adap}$ and $2.5t_{adap}$ was created based on the number of data points left in the trace.
725 Data for number of CW flagella n_{cw} from multiple cells with the same total number of flagella N
726 were pooled in each time window. The time-dependent histogram $p_{N,obs}(n_{cw}, t)$ was constructed
727 and the time-dependent [CheY-P] distribution $p_{fit}(y_P,t)$ was determined for each time window.
728 The error in $p_{fit}(y_P,t)$ was calculated by bootstrap resampling as before, over each time window.
729 We calculated a global [CheY-P] distribution for each time window across all N as described
730 above. For the results from this analysis reported in **Figure 4** and **5**, we used the beta distribution
731 trial function to estimate $p_{fit}(y_P,t)$.

732

733 **Analytical model of CheY-P noise with no CheA fluctuations**

734 We used a stochastic chemical kinetics approach to model CheY phosphorylation and CheY-P
735 dephosphorylation reactions of the *E. coli* chemotaxis network and determine the fluctuations in
736 CheY-P. While various models[56,57] describe a wider range of reactions in the chemotactic signaling
737 network, we chose the simplest possible scenario to verify that it could recapitulate the essential
738 features of our experimental results.

739 In our model, we considered the following chemical reaction,

740 $$\text{CheY} \underset{k_Z}{\overset{k_A a}{\rightleftharpoons}} \text{CheY-P} \quad (17)$$

741 where $k_A a$ is the rate of phosphorylation of CheY by the CheA-receptor complex, and k_Z is the
742 rate of dephosphorylation of CheY-P by the phosphatase CheZ. As is standard practice[57,58], we
743 defined the activity a of the CheA-receptor complex as the probability that it is in the active state

744 ($0 \le a \le 1$) and k_A as the maximum phosphorylation rate. We initially assumed that both $k_A a$ and

745 k_Z remain constant.

746 We used a chemical master equation (CME) approach to determine number fluctuations in

747 CheY-P for this set of reactions. The individual reactions in terms of the molecular species are:

748 Phosphorylation of CheY: $N_{Yp} \xrightarrow{k_A a (N_Y^{tot} - N_{Yp})} N_{Yp} + 1$

749 Dephosphorylation of CheY-P: $N_{Yp} \xrightarrow{k_Z N_{Yp}} N_{Yp} - 1$

750 where N_{Yp} is number of CheY-P molecules, and N_Y^{tot} is the total number of (unphosphorylated

751 and phosphorylated) CheY molecules, the latter assumed to be fixed. The CME corresponding

752 to these reactions is given by

753 $$\frac{dP_{N_{Yp}}}{dt} = k_A a (N_Y^{tot} - N_{Yp} + 1) P_{N_{Yp}-1} + k_Z (N_{Yp} + 1) P_{N_{Yp}+1} - \left[k_Z N_{y_p} + k_A a (N_Y^{tot} - N_{Yp}) \right] P_{N_{Yp}}, \quad (18)$$

754 where $P_{N_{Yp}}(t)$ is the probability that the number of CheY-P molecules at time t is N_{Yp}.

755 Following the approach of McQuarrie and Gillespie[59], the CME Eq. (18) can be solved

756 analytically to yield the following steady-state mean and variance in CheY-P number,

757 $$\langle N_{Yp} \rangle = \frac{k_A a}{k_A a + k_Z} N_Y^{tot}, \quad (19)$$

758 $$\sigma_{N_{Yp}}^2 = \frac{k_Z k_A a}{(k_A a + k_Z)^2} N_Y^{tot} = \langle N_{Yp} \rangle \left(1 - \frac{\langle N_{Yp} \rangle}{N_Y^{tot}} \right). \quad (20)$$

759 Eqs. (19) and (20) can be combined to obtain the coefficient of variation

760 $$\frac{\sigma_{N_{Yp}}^2}{\langle N_{Yp} \rangle^2} = \frac{1 - f_{Yp}}{\langle N_{Yp} \rangle}, \quad (21)$$

761 where $f_{Yp} \equiv \langle N_{Yp} \rangle / N_{Yp}^{tot}$ is the fraction of total CheY that is phosphorylated. Eq. (21) is the expected

762 result for a binomial-distributed process. Eq. (19) and (20) can be converted into expressions for

763 the mean and variance in CheY-P concentration by dividing by the *E. coli* cell volume V_C, assumed

764 to be 1.4 fL[60]: $\mu_{Yp} = \langle N_{Yp} \rangle / V_C$ and $\sigma_{Yp}^2 = \sigma_{N_{Yp}}^2 / V_C^2$.

765

Analytical model of CheY-P noise with CheA fluctuations

We next considered the same phosphorylation-dephosphorylation chemical reaction, Eq. (17), with temporal fluctuations in CheA activity. We devised a simple model in which CheA interconverts between active (ON) and inactive states (OFF) with rates $\lambda_A^{\pm}$,

$$\mathrm{CheA_{OFF}} \underset{\lambda_A^-}{\overset{\lambda_A^+}{\rightleftharpoons}} \mathrm{CheA_{ON}}. \tag{22}$$

The individual reactions in Eqs. (17) and (22) in terms of each molecular species are now:

Activation of CheA: $N_A \xrightarrow{\lambda_A^+(N_A^{tot}-N_A)} N_A+1$

Deactivation of CheA: $N_A \xrightarrow{\lambda_A^- N_A} N_A-1$

Phosphorylation of CheY: $N_{Yp} \xrightarrow{\kappa_A N_A (N_Y^{tot}-N_{Yp})} N_{Yp}+1$

Dephosphorylation of CheY-P: $N_{Yp} \xrightarrow{k_Z N_{Yp}} N_{Yp}-1$

where N_A and N_A^{tot} are the number of active CheA molecules and the total number of CheA molecules in the cell, respectively. Here, we made explicit the dependence of the phosphorylation rate on the number of active CheA, N_A, defining κ_A such that $\kappa_A N_A = k_A a$, with the activity $a = N_A / N_A^{tot}$ and the maximum phosphorylation rate $k_A = \kappa_A N_A^{tot}$.

From these reactions, the CME for both molecular species is given by:

$$\begin{aligned}\frac{dP_{N_A,N_{Yp}}}{dt} &= \lambda_A^+(N_A^{tot}-N_A+1)P_{N_A-1,N_{Yp}} + \lambda_A^-(N_A+1)P_{N_A+1,N_{Yp}} \\ &+\kappa_A N_A(N_Y^{tot}-N_{Yp}+1)P_{N_A,N_{Yp}-1} + k_Z(N_{Yp}+1)P_{N_A,N_{Yp}+1} \\ &-\left[\lambda_A^+(N_A^{tot}-N_A)+\lambda_A^-(N_A)+\kappa_A N_A(N_Y^{tot}-N_{Yp})+k_Z(N_{Yp})\right]P_{N_A,N_{Yp}}\end{aligned} \tag{23}$$

where $P_{N_A,N_{Yp}}(t)$ is the joint probability that there are N_A active CheA-receptor complexes and N_{Yp} CheY-P molecules at time *t*.

The reaction scheme in Eqs. (17) and (22) maps naturally into stochastic models of gene expression, where genes can switch from inactive to active (similar to CheA-receptor complexes), and active genes produce mRNA transcripts (similar to CheY phosphorylation). Paulsson[62,63] has developed a systematic formalism for calculating number fluctuations in gene expression, which

788 we adapted for our reaction scheme. The steady-state mean numbers of active CheA and CheY-
789 P are easily shown to be given by

790 $$\frac{\langle N_A \rangle}{N_A^{tot}} = a = \frac{\lambda_A^+}{\lambda_A^+ + \lambda_A^-}, \tag{24}$$

791 $$\frac{\langle N_{Yp} \rangle}{N_Y^{tot}} = f_{Yp} = \frac{k_A a}{k_A a + k_Z}, \tag{25}$$

792 where Eq. (25) is identical to Eq. (21) above, as expected. For number fluctuations, Paulsson
793 provides the following general solutions[63]:

794 $$\frac{\sigma_A^2}{\langle N_A \rangle^2} = \frac{1}{\langle N_A \rangle H_{AA}},$$

795 $$\frac{\sigma_{Yp}^2}{\langle N_{Yp} \rangle^2} = \frac{1}{\langle N_{Yp} \rangle H_{YY}} + \frac{\sigma_A^2}{\langle N_A \rangle^2}\left(\frac{H_{YA}}{H_{YY}}\right)^2 \frac{H_{YY}/T_Y}{H_{YY}/T_Y + H_{AA}/T_A},$$

796 where the logarithmic gains H_{ij} and times T_i are defined in Eq. (S5) and (S6) in Ref. [17]. Evaluating
797 these factors for the CME in Eq. (23), these expressions simplify into

798 $$\frac{\sigma_A^2}{\langle N_A \rangle^2} = \frac{1-a}{\langle N_A \rangle}, \tag{26}$$

799 which is expected for a binomial-distributed process, and

800 $$\frac{\sigma_{Yp}^2}{\langle N_{Yp} \rangle^2} = \frac{1-f_{Yp}}{\langle N_{Yp} \rangle}\left(1 + \frac{\langle N_{Yp} \rangle}{\langle N_A \rangle}\frac{\tau_A}{\tau_A + \tau_Y}(1-a)(1-f_{Yp})\right), \tag{27}$$

801 where $\tau_A = (\lambda_A^+ + \lambda_A^-)^{-1}$ is the characteristic relaxation timescale for CheA activation-deactivation,
802 and $\tau_Y = (k_A a + k_Z)^{-1}$ is the timescale for CheY phosphorylation-dephosphorylation. Note that in
803 the absence of CheA noise, Eq. (21) is recovered from Eq. (27).

804 From the steady-state solutions for the means of the molecular species, Eq. (24) and (25), we
805 obtained, after some algebra

806 $$\frac{\sigma_{Yp}^2}{\langle N_{Yp} \rangle^2} = \frac{1-f_{Yp}}{\langle N_{Yp} \rangle}\left[1 + \langle b \rangle\left(1 - \frac{f_{Yp}}{\alpha}\right)\right], \tag{28}$$

807 in which we defined $\alpha \equiv k_A / (k_A + k_Z)$ and $\langle b \rangle \equiv N_Y^{tot} k_A \tau_{eff} / N_A^{tot}$, and where $\tau_{eff} = (\tau_A^{-1} + \tau_Y^{-1})^{-1}$. We
808 note that the first factor in Eq. (28) is the coefficient of variation in the absence of CheA
809 fluctuations. The second factor describes how CheA noise increases CheY-P number fluctuations.
810 In analogy with transcriptional bursting[64,65], the parameter $\langle b \rangle$ represents the "burst size", the
811 number of new CheY-P molecules generated per CheA within its active lifetime. The other
812 parameter, α, describes the effect of a kinetic ceiling of CheA on CheY-P number fluctuations.
813 f_{Yp} / α is the number of CheY-P molecules when all CheA-receptor complexes are active (a = 1),
814 i.e. when the system phosphorylates at its maximum possible rate. When CheA-receptor
815 complexes attain this kinetic ceiling, the added CheY-P fluctuations due to CheA noise drops to
816 zero in Eq. (28), as expected from Eq. (26).

817 **Table 1**

818 Strains and Plasmids used in this study

Strain	Genotype	Comments	Source
HCB1613	*fliC*::Tn5 (Kan^R)	wild type "deleted" for fliC	Gift of Berg lab
HCB1660	*fliC*::Tn5 (Kan^R)	wild type "deleted" for fliC expressing pBAD33- $fliC^{S219C}$	Gift of Berg lab
RB01	*cheZ*::Cm, *fliC*::Tn5 (Kan^R)	N/A	This work
RB02	*cheZ*::FRT, *fliC*::Tn5 (Kan^R)	N/A	This work
RB03	*cheZ*::FRT, *fliC*::Tn5 (Kan^R)	wild type "deleted" for fliC and cheZ expressing pBAD33- $fliC^{S219C}$	This work
Plasmids			
pKD3		Template for Cm^R cassette	[67]
pKD46		Plasmid expressing λ Red recombinases	[67]
pCP20		Plasmid expressing Flp recombinase	[67]
pBAD33	$fliC^{S219C}$ under P_{araBAD} promoter, Cm^R, p15a origin	Expresses mutant version of FliC for fluorescence labelling	[66]gift of Berg lab

819

820 **Table 2**

821 Primers used in this work

Primer	Sequence
CheZ-pKDF	GGAAAAACTCAACAAAATCTTTGAGAAACTGGGCATGTGAG

	GATGCGACTGTGTAGGCTGGAGCTGCTTC
CheZ-pKDR	TTATCAGACCGCCTGATATGACGTGGTCACGCCACATCAGGC AATACAAACATATGAATATCCTCCTTA

822

823 **Table 3**

824 Distribution and fitting parameters for the [CheY] distribution $p_{fit}(y_P/K)$ for the wild type strain
825 with different trial functions

Distri-bution	Parameter	$N = 2$	$N = 3$	$N = 4$	$N = 5$	Global
Beta	μ_{y_p}/K	0.84 ± 0.02	0.80 ± 0.04	0.70 ± 0.06	0.86 ± 0.03	0.80 ± 0.02
	σ_{y_p}/K	0.16 ± 0.02	0.17 ± 0.02	0.20 ± 0.03	0.12 ± 0.02	0.17 ± 0.02
	Reduced χ^2	Undefined	1.9	7.4	5.4	6.7
Gauss	μ_{y_p}/K	0.86 ± 0.02	0.83 ± 0.02	0.77 ± 0.04	0.88 ± 0.03	0.83 ± 0.02
	σ_{y_p}/K	0.13 ± 0.01	0.12 ± 0.01	0.13 ± 0.02	0.11 ± 0.03	0.13 ± 0.02
	Reduced χ^2	Undefined	0.63	12.6	5.1	6.7
Gamma	μ_{y_p}/K	0.83	0.81	0.73	0.85	0.78
	σ_{y_p}/K	0.19	0.18	0.18	0.19	0.18
	Reduced χ^2	Undefined	39.5	44.1	56	9.9

826

827 **Table 4**

828 Distribution parameters for the [CheY] distribution $p_{fit}(y_P)$ for the wild type strain

N	Mean [CheY-P], μ_{y_p}/K	Standard deviation in [CheY-P], σ_{y_p}/K	Coefficient of Variation, σ_{y_p}/μ_{y_p}
2	0.84 ± 0.02	0.16 ± 0.02	0.19 ± 0.02

3	0.80 ± 0.04	0.17 ± 0.02	0.21 ± 0.04
4	0.70 ± 0.06	0.20 ± 0.03	0.29 ± 0.07
5	0.86 ± 0.03	0.12 ± 0.02	0.14 ± 0.03
Global	0.80 ± 0.02	0.17 ± 0.02	0.22 ± 0.03

Table 5

Distribution parameters for the [CheY] distribution $p_{fit}(y^*)$ for the mutant CheY* strain

N	Mean [CheY-P], μ_{y^*}/K	Standard deviation in [CheY-P], σ_{y^*}/K	Coefficient of Variation, σ_{y^*}/μ_{y^*}
2	0.94 ± 0.04	0.13 ± 0.04	0.14 ± 0.04
3	0.93 ± 0.02	0.06 ± 0.01	0.06 ± 0.02
4	0.91 ± 0.02	0.06 ± 0.02	0.06 ± 0.02
5	0.84 ± 0.04	0.09 ± 0.03	0.11 ± 0.04
Global	0.90 ± 0.02	0.10 ± 0.02	0.11 ± 0.02

Appendix

Sensitivity of [CheY-P] distribution to experimental parameters

We note that while $p(c)$ in Eq. (1) is determined exactly from the experimental data $p_N(n_{cw})$ with no additional input parameters, $p(y_P)$ in Eq. (4) depends on the values of the experimental parameters y_{tot}, K, and H. While y_{tot} is well known[44], values of K and H may vary due to flagellar motor remodeling as well as differences between individual motors or cells (described in detail in the following sections). In this section, we describe the sensitivity of the inferred [CheY-P] distribution on y_{tot}, K, and H.

As mentioned in the text, the integral Eq. (4) is insensitive to the exact value of y_{tot}. Because the CW bias $c \approx 1$ for $y_P > K$ due to the sigmoidicity of Eq. (3), the integral depends very weakly on the precise value of the upper limit, and y_{tot} can be replaced with ∞ with an error on the integral value <0.01%. In contrast, the dependence of Eq. (4) on K and H is more significant and may affect our inference of [CheY-P] fluctuations. We analyzed the sensitivity of the mean [CheY-P], μ_{y_p}, and coefficient of variation, σ_{y_p}/μ_{y_p}, on these two experimental parameters.

Making use of Eq. (3) and (4), the moments of the distribution $p(y_P)$ may be written as:

$$\left\langle y_P^m \right\rangle = \int_0^\infty dy_P\, y_P^m p(y_P) = \int_0^1 dc\, K^m \left(\frac{c}{1-c} \right)^{\frac{m}{H}} p(c) \tag{29}$$

To estimate the sensitivity of the moments to K and H, we determined their logarithmic gains. For K, it is easy to show that

$$\frac{d \ln \left\langle y_P^m \right\rangle}{d \ln K} = m\,,$$

which indicates that $\mu_{y_P} = \langle y_P \rangle$ scales as K, $\sigma_{y_P}^2 = \left\langle y_P^2 \right\rangle - \langle y_P \rangle^2$ scales as K^2, and σ_{y_P}/μ_{y_P} is independent of K. For H,

$$\frac{d \left\langle y_P^m \right\rangle}{d \ln H} = -\frac{m}{H} K^m \int_0^1 dc \left(\frac{c}{1-c} \right)^{\frac{m}{H}} \ln\left(\frac{c}{1-c} \right) p(c) = -m \int_0^\infty dy_P\, y_P^m \ln\left(\frac{y_P}{K} \right) p(y_P)\,,$$

which cannot be solved analytically. However, since the distributions $p(y_P)$ are peaked functions (see **Figures 2 and supplements**, **Figure 4**), the right integral is well approximated by a Taylor

expansion about the mean [CheY-P], $\langle y_P \rangle = \mu_{y_P}$. Defining the function $f_m(y_P) \equiv -m y_P^m \ln(y_P / K)$ in the integrand, it follows that, to lowest two orders:

$$\frac{d\langle y_P^m \rangle}{d\ln H} = \langle f_m(y_P) \rangle \approx f_m(\mu_{y_P}) + \frac{1}{2} f_m''(\mu_{y_P}) \sigma_{y_P}^2 ,$$

where ” denotes the second derivative with respect to y_P. After some algebra, the sensitivity of μ_{y_P} to H can be shown to be approximately

$$\frac{d\ln \mu_{y_P}}{d\ln H} \approx -\ln \frac{\mu_{y_P}}{K} , \tag{30}$$

which ranges between 0.4 and 0 for the range of values observed experimentally for μ_{y_P}/K, 0.7 to 1 (**Figure 5c**). The sensitivity of σ_{y_P} to H is given by

$$\frac{d\ln \sigma_{y_P}}{d\ln H} \approx -\left(1 + \ln \frac{\mu_{y_P}}{K}\right), \tag{31}$$

which ranges between -0.65 to -1 for the same range of values of μ_{y_P}. Subtracting Eq. (30) from Eq. (31) gives an expression for the coefficient of variation and shows that σ_{y_P}/μ_{y_P} approximately scales as H^{-1}. These dependences match those obtained by directly integrating Eq. (4) numerically while varying H. In summary, our sensitivity analysis indicates that μ_{y_P} scales linearly with K but does not depend very strongly on H, whereas σ_{y_P}/μ_{y_P} is independent of K but scales inversely with H. Neither parameter depends appreciably on y_{tot}.

Effect of flagellar motor remodeling on CheY-P distribution

Studies have shown that the flagellar motor exhibits adaptive remodeling[45–47]. FliM, a component of the switch complex at the base of the flagellar motor that binds CheY-P, is dynamic and able to bind to or dissociate from the motor. Furthermore, the mean number of FliM molecules bound to the motor depends on its CW bias. As a result, changes in motor bias—either from temporal fluctuations or in response to a chemotactic stimulus—lead to FliM exchange and motor remodeling. This in turn affects the binding of CheY-P to the motor, which shifts the motor’s CW bias, leading to a negative feedback loop and an adaptive response.

Zhang et al. recently developed a quantitative model for this dynamic process[43], using the Monod-Wyman-Changeux (MWC) model to describe the dependence of the motor's CW bias c on the number of bound FliM molecules, N_F, and intracellular [CheY-P], y_P:

$$c(y_P, N_F) = \frac{1}{1 + e^{(N_F g(y_P) + \varepsilon)/k_B T}}, \tag{32}$$

where $\varepsilon = 33.65\ k_B T$ and

$$g(y_P) = k_B T \ln\left(\frac{1 + y_P / K_2}{1 + y_P / K_1}\right), \tag{33}$$

and where K_2 = 7.5 μM and K_1 = 1.28 μM. Eqs. (32)-(33) describe a function that is nearly indistinguishable in shape to the Hill curve $c(y_P)$, Eq. (3), first determined by Cluzel et al.[25], despite their different analytical forms. For a value of N_F = 43.5 (corresponding to our experimentally determined $c(y_P)$ as detailed later in this section), Eqs. (32)-(33) correspond to a Hill curve with parameters H = 18 and K = 2.4 μM. (Note also that $\sqrt{K_1 K_2} = K$ = 3.1 μM [43]).

In Zhang et al., motor remodeling is described by the differential equation[43]:

$$\frac{dN_F}{dt} = k_{on}(N_{F,\max} - N_f) - k_{off}(N_F - N_{F,NE}(c)). \tag{34}$$

The FliM association and dissociation dynamics are slow, and given by rate constants k_{on} and k_{off} with similar values of ~0.02 s^{-1} (Lele et al., 2012). FliM bound to the switch complex can adopt two different states, an unstable state that freely exchanges with cytoplasmic FliM, and a stable non-exchanging state whose number is denoted by $N_{F,NE}$ in Eq. (34)[43]. $N_{F,NE}$ is a linear function of the CW bias, adopting a value of 34 for a motor rotating CCW and a value of 12 for one rotating CW[43], i.e. $N_{F,NE}(c) = 34 - 22c$. $N_{F,max}$ = 56 represents the maximum number of FliM binding sites on the motor.

We used the above model to determine the effect of motor remodeling on our estimates of noise in the chemotaxis network. We can predict qualitatively the effect of the negative feedback loop generated by remodeling. Given a small increase in CheY-P level above the steady state, the CW bias c increases from Eqs. (32) and (33), and the bound FliM number N_F in turn decreases from Eq. (34). A decrease in N_F leads to a shift in the curve $c(y_P, N_F)$ to the right according to Eq. (32), which decreases c. Thus, for a fixed increase in CheY-P, the net effect of the adaptive

remodeling is to suppress corresponding changes in c. In turn, to reproduce the observed fluctuations in c in our data, a larger variance in [CheY-P] must be assumed in the presence of motor remodeling compared to in its absence. We thus expect that ignoring remodeling leads to an underestimate of the CheY-P fluctuations.

The magnitude of this underestimate will depend on the timescale of CheY-P fluctuations relative to that of remodeling. Due to the slow remodeling dynamics (of timescale $1/k_{off} \approx 50$ s), the remodeling feedback loop will not respond to fast CheY-P fluctuations. To model the effect of remodeling on CheY-P noise estimates, we carried out numerical simulations of CheY-P fluctuations using a discretized Langevin equation

$$y_P(t+dt) = y_P(t) - \frac{1}{\tau_A}(y_P(t) - \mu_{Yp})dt + \sigma_{Yp}\sqrt{\frac{2dt}{\tau_A}}\xi(t)\,, \tag{35}$$

where τ_A is the characteristic timescale for fluctuations in [CheY-P] due to CheA activation-deactivation, ξ are Gaussian-distributed random numbers with unit variance, and μ_{y_p} and σ_{y_p} are the mean and standard deviation of the [CheY-P], respectively. [Note that by construction Eq. (35) generates a Gaussian [CheY-P] distribution. However, in the main text, we utilize a beta distribution as a trial distribution to estimate [CheY-P] fluctuations. For the sake of consistency, in the following analysis we compare the simulation results to [CheY-P] fluctuations in the absence of remodeling assuming a Gaussian [CheY-P] distribution (see **Figure 2 – figure supplement 2**), a trial distribution that also works well to estimate [CheY-P] fluctuations (**see Table 3**).]

Using $y_p(t)$ generated by Eq. (35) as input to Eqs. (32)-(34), we simulated remodeling motors at steady state, with the time-dependent CW bias $c(t)$ and number of bound FliM $N_F(t)$ as outputs. We used $N_F(t = 0) = N_{F,NE}(c(\mu_{y_p}))$ as the initial condition for Eq. (35), although simulation results were insensitive to this value at long times, and ran multiple (N = 200) repeats of the simulation. μ_{y_p} and σ_{y_p} were adjusted so that the mean and standard deviation in CW bias matched the values we determined experimentally for cells at steady state, $\mu_c = 0.14$ and $\sigma_c = 0.22$. **Appendix – figure 1a** plots the coefficient of variation, σ_{y_p}/μ_{y_p}, required to reproduce the experimental CW bias parameters in the presence of remodeling, as a function of the CheY-P fluctuation timescale τ_A.

934 As expected, when $\tau_A << 1/k_{off}$, the effect of remodeling on CheY-P fluctuation estimates is
935 minimal. In contrast, when $\tau_A \approx 1/k_{off}$, CheY-P fluctuations must increase to match the
936 experimental data; however, the underestimate in CheY-P noise is moderate, <25% for $\tau_A \approx 10$ s,
937 which is thought to be the timescale of CheY-P fluctuations due CheR-CheB dynamics[32,33].
938 Additionally, we found $N_f(t \to \infty) = 43.5$ to correspond to experimentally determined CW bias
939 mean and standard deviation values across all τ_A.

940 We also used this framework to simulate cells undergoing chemotactic adaptation in
941 response to a step down in MeAsp from 1 to 0 mM. Here, we did not model adaptation kinetics
942 explicitly. Instead we used the experimentally measured mean and standard deviation in CW bias
943 in ~2.5-s time windows post-stimulus (corresponding to windows of duration $0.2t_{adap}$, see **Figure**
944 **4**) to guide piecewise simulations over those time windows. Briefly, the appropriate values for
945 μ_{y_p} and σ_{y_p} in Eq. (35) were selected to generate a time trace $c(t)$ with μ_c and σ_c matching the
946 experimental data in each time window. As above, we ran multiple (N = 5000) repeats of the
947 simulations in each time window. The steady-state value of N_F = 43.5 served as the initial
948 condition for simulations in the first time window post-stimulus. $N_F(t)$ evolved over each time
949 window, and its average over the simulation repeats at the end of each time window served as
950 the initial condition for the next time window.

951 **Appendix – figure 1b and 1c** plot the mean μ_{y_p} and coefficient of variation σ_{y_p}/μ_{y_p} vs. time
952 post-stimulus in the absence and presence of remodeling (for τ_A = 10 s only). Again, a moderate
953 increase of <15% in CheY-P noise is observed as a result of accounting for motor remodeling. The
954 larger effect is seen on the mean CheY-P, which increases as a consequence of the adaptive effect
955 of remodeling, as described above. Briefly, the increase in c due to the stimulus is followed by a
956 decrease in N_F which shifts the curve $c(y_P, N_F)$ to the right. As a result, a larger value of μ_{y_p} is
957 necessary to produce the same value for μ_c in the absence of remodeling.

958 Finally, **Appendix – figure 1d** plots the coefficient of variation σ_{y_p}/μ_{y_p} vs. the mean μ_{y_p} for
959 steady state and post-stimulus in the absence and presence of remodeling (for τ_A = 10 s only). Eq.
960 (8) in the main text is used to fit both sets of data (R^2 = 0.7 in absence of remodeling and R^2 = 0.8
961 in presence of remodeling). While the values of the kinetic ceiling α are identical in absence and

presence of remodeling (α = 0.246 ± 0.008 and α = 0.246 ± 0.002 respectively), the burst size <*b*> is somewhat different (161 ± 110 and 271 ± 114 respectively).

Effect of motor-to-motor differences on CheY-P distribution

In Eqs. (4)-(5) of the main text, we implicitly assumed that the CW bias vs. CheY-P relation, Eq. (3), is the same for all motors, i.e. the parameters *K* and *H* are constants. However, there may be differences between motors that lead to variations in these parameters. Recent work[71] has shown that the load on the flagellar motors shifts the curve midpoint, *K*. Thus, differences in load (e.g. from different flagellar lengths) could lead to variation in CW bias across motors for the same intracellular [CheY-P].

To estimate the variation in *c* vs. y_P curves across motors of the same cell, we analyzed time traces from cells of the CheY* strain. Since we could identify each flagellum during our fluorescence movies, we determined the time-averaged CW bias of each motor individually and quantified CW bias differences across motors on the same cell. As CheY* expression is controlled, its concentration is assumed to be constant over the time scale of the measurements (30-40 s) for each individual cell. Variations in CW bias thus represent either statistical fluctuations or differences in *K* between motors (Differences in *H* are expected to have a negligible effect on average CW bias). From Eq. (3), the CW bias c_i of the *i*-th motor gives the ratio K_i/y^*, where $y^* \equiv$ [CheY*] is constant. Normalizing this ratio by its average over all motors on the same cell yields $K_i / \langle K \rangle$, the distribution of which over all cells provides an upper bound for the coefficient of variation in *K* of 3%.

We next determined the effect of a variation in *K* on the estimated CheY-P fluctuations. If there exist motor-to-motor differences, then Eq. (2) connecting the CheY-P distribution to the probability $p_N(n_{cw})$ that n_{CW} flagella rotate CW must be modified by replacing the conditional probability $p_N(n_{cw} \mid c)$ with the corresponding equation for non-identical motors:

$$p_N(n_{cw} \mid \{c_i\}) = \sum_{\sigma} \prod_{i=1}^{n_{cw}} c_{\sigma(i)} \prod_{j=n_{cw}+1}^{N} (1 - c_{\sigma(j)}), \tag{36}$$

where the sum is carried out over all non-identical permutations σ of the motor index and where

989 $$c_i = \frac{y_P^H}{K_i^H + y_P^H}\,. \tag{37}$$

990 We carried out numerical simulations of cells with N flagellar motors each with a different K_i
991 drawn from a Gaussian distribution with mean 2.4 μM and coefficient of variation 5% (larger than
992 our upper bound estimate of 3% above). For each simulated cell, we generated a probability
993 $p_{N,sim}(n_{cw})$ using Eq. (4) with Eqs. (36) and (37), assuming a common CheY-P distribution $p_{in}(y_P)$
994 with mean μ_{y_p} = 1.97 μM and coefficient of variation σ_{y_p}/μ_{y_p} = 0.15 as input (these values
995 correspond to the CheY-P Gaussian distribution parameters determined for wild type HCB1660
996 cells). We then fitted the $p_{N,sim}(n_{cw})$ with a trial distribution function $p_{fit}(y_P)$, according to the
997 procedure outlined in the main text, assuming identical motors, i.e. Eqs. (4)-(5). Comparing the
998 input and fit distributions, $p_{in}(y_P)$ and $p_{fit}(y_P)$, allowed us to quantify the effect of assuming
999 identical motors in cells with non-identical motors. For a motor-to-motor variation of 5% in K, we
1000 found that μ_{y_p} was 2.1 μM and the coefficient of variation σ_{y_p}/μ_{y_p} decreased by ~25%.
1001

1002 ## Effect of cell-to-cell variation on CheY-P distribution

1003 We also explored the effect of variation in the c vs. y_P curves between cells. Similarly to above,
1004 we estimated variations in the parameter K across a wild-type cell population by determining the
1005 time-averaged CW bias of individual cells and quantifying cell-to-cell differences CW bias. This
1006 analysis provides an upper bound for the population coefficient of variation in K of <5%. We next
1007 carried out numerical simulations of cells each with a different K_i drawn from a Gaussian
1008 distribution with mean 2.4 μM and coefficient of variation 5%. We then quantified the effect of
1009 assuming an identical value of K for a population of cells in which this parameter varied. Assuming
1010 a common CheY-P distribution $p_{in}(y_P)$ with mean μ_{y_p} = 1.97 μM and coefficient of variation σ_{y_p}/μ_{y_p}
1011 = 0.15 as input, for a cell-to-cell variation of 5% in K, we found that the mean [CheY-P] was 1.97
1012 μM and the coefficient of variation remained unchanged or increased marginally by ~5%. The
1013 increase in estimated [CheY-P] fluctuations is similar to that observed with CheY* cells, when
1014 comparing population and single-cell level distributions (**Figure 2** and **3**). Cell-to-cell variation in

1015 CheY^{D13K} expression in the CheY* strain, equivalent to variation in *K*, broadens the observed
1016 [CheY-P] distribution.

1017 ## References

1018 1. Lim WA, Mayer B., P. T. *Cell Signaling*. (Garland Science, 2014).

1019 2. Mcadams, H. H. & Arkin, A. Stochastic mechanisms in gene expression. *Proc. Natl. Acad.*
1020 *Sci. U. S. A.* **94**, 814–819 (1997).

1021 3. Allen, C. & Stevens, C. F. An evaluation of causes for unreliability of synaptic
1022 transmission. *Proc. Natl. Acad. Sci. U. S. A.* **91**, 10380–10383 (1994).

1023 4. Barkai, N. & Leibler, S. Robustness in simple biochemical networks to transfer and
1024 process information. *Nature* **387**, 913–917 (1997).

1025 5. Silva-Rocha, R. & de Lorenzo, V. Noise and Robustness in Prokaryotic Regulatory
1026 Networks. *Annu. Rev. Microbiol.* **64**, 257–275 (2010).

1027 6. Stelling, J., Sauer, U., Szallasi, Z., Doyle, F. J. & Doyle, J. Robustness of Cellular Functions.
1028 *Cell* **118**, 675–685 (2004).

1029 7. Eldar, A. *et al.* Robustness of the BMP morphogen gradient in Drosophila embryonic
1030 patterning. *Nature* **419**, 304–308 (2002).

1031 8. Rao, C. V, Wolf, D. M. & Arkin, A. P. Control, exploitation and tolerance of intracellular
1032 noise. *Nature* **420**, 231–237 (2002).

1033 9. Tsimring, L. S. Noise in biology. *Reports Prog. Phys.* **77**, (2014).

1034 10. Raj, A. & van Oudenaarden, A. Nature, nurture, or chance: stochastic gene expression
1035 and its consequences. *Cell* **135**, 216–26 (2008).

1036 11. Eldar, A. & Elowitz, M. B. Functional roles for noise in genetic circuits. *Nature* **467**, 167–
1037 173 (2010).

1038 12. Balázsi, G., Van Oudenaarden, A. & Collins, J. J. Cellular decision making and biological
1039 noise: From microbes to mammals. *Cell* **144**, 910–925 (2011).

1040 13. Wadhams, G. H. & Armitage, J. P. Making sense of it all: bacterial chemotaxis.

1041 *Nat.Rev.Mol.Cell Biol.* **5**, 1024–1037 (2004).

1042 14. Shimizu, T. S., Tu, Y. & Berg, H. C. A modular gradient-sensing network for chemotaxis in
1043 Escherichia coli revealed by responses to time-varying stimuli. *Mol. Syst. Biol.* **6**, 1–14
1044 (2010).

1045 15. Lan, G., Schulmeister, S., Sourjik, V. & Tu, Y. Adapt locally and act globally: Strategy to
1046 maintain high chemoreceptor sensitivity in complex environments. *Mol. Syst. Biol.* **7**, 1–
1047 16 (2011).

1048 16. Sourjik, V. & Wingreen, N. S. Responding to chemical gradients: bacterial chemotaxis.
1049 *Curr. Opin. Cell Biol.* **24**, 262–8 (2012).

1050 17. Micali, G. & Endres, R. G. Bacterial chemotaxis: Information processing, thermodynamics,
1051 and behavior. *Curr. Opin. Microbiol.* **30**, 8–15 (2016).

1052 18. Larsen, S. H., Reader, R. W., Kort, E. N., Tso, W. W. & Adler, J. Change in direction of
1053 flagellar rotation is the basis of the chemotactic response in Escherichia coli. *Nature* **249**,
1054 74–77 (1974).

1055 19. Macnab, R. M. & Ornston, M. K. Normal-to-curly flagellar transitions and their role in
1056 bacterial tumbling. Stabilization of an alternative quaternary structure by mechanical
1057 force. *J. Mol. Biol.* **112**, 1–30 (1977).

1058 20. Turner, L., Ryu, W. S. & Berg, H. C. Real-time imaging of fluorescent flagellar filaments. *J.*
1059 *Bacteriol.* **182**, 2793–2801 (2000).

1060 21. Darnton, N. C., Turner, L., Rojevsky, S. & Berg, H. C. On torque and tumbling in swimming
1061 Escherichia coli. *J. Bacteriol.* **189**, 1756–1764 (2007).

1062 22. Parkinson, J. S., Hazelbauer, G. L. & Falke, J. J. Signaling and sensory adaptation in
1063 Escherichia coli chemoreceptors: 2015 update. *Trends Microbiol.* **23**, 257–266 (2015).

1064 23. Scharf, B. E., Fahrner, K. A., Turner, L. & Berg, H. C. Control of direction of flagellar
1065 rotation in bacterial chemotaxis. *Proc. Natl. Acad. Sci.* **95**, 201–206 (1998).

1066 24. Alon, U. *et al.* Response regulator output in bacterial chemotaxis. *EMBO J.* **17**, 4238–4248
1067 (1998).

1068 25. Cluzel, P., Surette, M. & Leibler, S. An Ultrasensitive Bacterial Motor Revealed by
1069 Monitoring Signaling Proteins in Single Cells. *Science (80-.).* **287**, 1652–1655 (2000).

1070 26. Hess, J. F., Oosawa, K., Kaplan, N. & Simon, M. I. Phosphorylation of three proteins in the
1071 signaling pathway of bacterial chemotaxis. *Cell* **53**, 79–87 (1988).

1072 27. Blat, Y. & Eisenbach, M. Phosphorylation-Dependent Binding of the Chemotaxis Signal
1073 Molecule CheY to Its Phosphatase, CheZ. *Biochemistry* **33**, 902–906 (1994).

1074 28. Springer, M. S., Goy, M. F. & Adler, J. Protein methylation in behavioural control
1075 mechanisms and in signal transduction. *Nature* **280**, 279–284 (1979).

1076 29. Kehry, M. R., Bond, M. W., Hunkapiller, M. W. & Dahlquist, F. W. Enzymatic deamidation
1077 of methyl-accepting chemotaxis proteins in Escherichia coli catalyzed by the cheB gene
1078 product. *Proc. Natl. Acad. Sci. U. S. A.* **80**, 3599–3603 (1983).

1079 30. Borkovich, K. A., Alex, L. A. & Simon, M. I. Attenuation of sensory receptor signaling by
1080 covalent modification. *Proc. Natl. Acad. Sci.* **89**, 6756–6760 (1992).

1081 31. Korobkova, E., Emonet, T., Vilar, J. M. G., Shimizu, T. S. & Cluzel, P. From molecular noise
1082 to behavioural variability in a single bacterium. *Nature* **428**, 574–578 (2004).

1083 32. Colin, R., Rosazza, C., Vaknin, A. & Sourjik, V. Multiple sources of slow activity
1084 fluctuations in a bacterial chemosensory network. *Elife* **6**, 1–32 (2017).

1085 33. Keegstra, J. M. *et al.* Phenotypic diversity and temporal variability in a bacterial signaling
1086 network revealed by single-cell FRET. *Elife* **6**, 1–33 (2017).

1087 34. Matthäus, F., Jagodič, M. & Dobnikar, J. E. coli superdiffusion and chemotaxis-search
1088 strategy, precision, and motility. *Biophys. J.* **97**, 946–957 (2009).

1089 35. Emonet, T. & Cluzel, P. Relationship between cellular response and behavioral variability
1090 in bacterial chemotaxis. *Proc. Natl. Acad. Sci. U. S. A.* **105**, 3304–3309 (2008).

1091 36. He, R., Zhang, R. & Yuan, J. Noise-Induced Increase of Sensitivity in Bacterial Chemotaxis.
1092 *Biophys. J.* **111**, 430–437 (2016).

1093 37. Flores, M., Shimizu, T. S., ten Wolde, P. R. & Tostevin, F. Signaling Noise Enhances
1094 Chemotactic Drift of E. coli. *Phys. Rev. Lett.* **109**, 148101 (2012).

1095 38. Terasawa, S. *et al.* Coordinated reversal of flagellar motors on a single Escherichia coli
1096 cell. *Biophys. J.* **100**, 2193–2200 (2011).

1097 39. Mears, P. J., Koirala, S., Rao, C. V., Golding, I. & Chemla, Y. R. Escherichia coli swimming is
1098 robust against variations in flagellar number. *Elife* **3**, 1–18 (2014).

1099 40. Min, T. L. *et al.* High-resolution, long-term characterization of bacterial motility using
1100 optical tweezers. *Nat. Methods* **6**, 831–835 (2009).

1101 41. Park, H. *et al.* Interdependence of behavioural variability and response to small stimuli in
1102 bacteria. *Nature* **468**, 819–821 (2010).

1103 42. Min, T. L., Mears, P. J., Golding, I. & Chemla, Y. R. Chemotactic adaptation kinetics of
1104 individual Escherichia coli cells. *Proc. Natl. Acad. Sci.* **109**, 9869–9874 (2012).

1105 43. Zhang, C., He, R., Zhang, R. & Yuan, J. Motor Adaptive Remodeling Speeds Up Bacterial
1106 Chemotactic Adaptation. *Biophys. J.* **114**, 1225–1231 (2018).

1107 44. Li, M. & Hazelbauer, G. L. Cellular stoichiometries of the components of the chemotaxis
1108 signaling complex. *J. Bacteriol* **186**, 3687–3694 (2004).

1109 45. Yuan, J., Branch, R. W., Hosu, B. G. & Berg, H. C. Adaptation at the output of the
1110 chemotaxis signalling pathway. *Nature* **484**, 233–236 (2012).

1111 46. Lele, P. P., Branch, R. W., Nathan, V. S. J. & Berg, H. C. Mechanism for adaptive
1112 remodeling of the bacterial flagellar switch. *Proc. Natl. Acad. Sci. U. S. A.* **109**, 20018–
1113 20022 (2012).

1114 47. Yuan, J. & Berg, H. C. Ultrasensitivity of an adaptive bacterial motor. *J. Mol. Biol.* **425**,
1115 1760–1764 (2013).

1116 48. Shamir, M., Bar-On, Y., Phillips, R. & Milo, R. SnapShot: Timescales in Cell Biology. *Cell*
1117 **164**, 1302-1302.e1 (2016).

1118 49. Tu, Y. & Grinstein, G. How White Noise Generates Power-Law Switching in Bacterial
1119 Flagellar Motors. **208101**, 1–4 (2005).

1120 50. Alon, U., Surette, M. G., Barkai, N. & Leibler, S. Robustness in bacterial chemotaxis.
1121 *Nature* **397**, 168–171 (1999).

1122 51. Sourjik, V. & Berg, H. C. Receptor sensitivity in bacterial chemotaxis. *Proc. Natl. Acad. Sci.*
1123 *U. S. A.* **99**, 123–127 (2002).

1124 52. Segall, J. E., Block, S. M. & Berg, H. C. Temporal comparisons in bacterial chemotaxis.
1125 *Proc. Natl. Acad. Sci. U. S. A.* **83**, 8987–8991 (1986).

1126 53. Block, S. M., Segall, J. E. & Berg, H. C. Adaptation kinetics in bacterial chemotaxis. *J.*
1127 *Bacteriol.* **154**, 312–323 (1983).

1128 54. Mesibov, R. & Adler, J. Chemotaxis toward amino-acids in Escherichia coli. *J. Bacteriol.*
1129 **112**, 315–326 (1972).

1130 55. Mesibov, R., Ordal, G. W. & Adler, J. The range of attractant concentrations for bacterial
1131 chemotaxis and the threshold and size of response over this range. Weber law and
1132 related phenomena. *J. Gen. Physiol.* **62**, 203–223 (1973).

1133 56. Vladimirov, N., Løvdok, L., Lebiedz, D. & Sourjik, V. Dependence of bacterial chemotaxis
1134 on gradient shape and adaptation rate. *PLoS Comput. Biol.* **4**, (2008).

1135 57. Bitbol, A. F. & Wingreen, N. S. Fundamental constraints on the abundances of chemotaxis
1136 proteins. *Biophys. J.* **108**, 1293–1305 (2015).

1137 58. Clausznitzer, D., Oleksiuk, O., Løvdok, L., Sourjik, V. & Endres, R. G. Chemotactic response
1138 and adaptation dynamics in Escherichia coli. *PLoS Comput. Biol.* **6**, 1–11 (2010).

1139 59. Mcquarrie, D. A. & Gillespie, D. T. Stochastic Theory and Simulations of Chemical Kinetics.
1140 *J. Appl. Probab.* **478**, 413–478 (1967).

1141 60. Sourjik, V. & Berg, H. C. Binding of the Escherichia coli response regulator CheY to its
1142 target measured in vivo by fluorescence resonance energy transfer. *Proc. Natl. Acad. Sci.*
1143 *U. S. A.* **99**, 12669–12674 (2002).

1144 61. Tindall, M. J., Porter, S. L., Wadhams, G. H., Maini, P. K. & Armitage, J. P. Spatiotemporal
1145 modelling of CheY complexes in Escherichia coli chemotaxis. *Prog. Biophys. Mol. Biol.*
1146 **100**, 40–46 (2009).

1147 62. Paulsson, J. Summing up the noise in gene networks. *Nature* **427**, 415–8 (2004).

1148 63. Paulsson, J. Models of stochastic gene expression. *Phys. Life Rev.* **2**, 157–175 (2005).

1149 64. Golding, I., Paulsson, J., Zawilski, S. M. & Cox, E. C. Real-time kinetics of gene activity in
1150 individual bacteria. *Cell* **123**, 1025–1036 (2005).

1151 65. Thattai, M. & van Oudenaarden, A. Intrinsic noise in gene regulatory networks. *Proc.*
1152 *Natl. Acad. Sci.* **98**, 8614–8619 (2001).

1153 66. Turner, L., Zhang, R., Darnton, N. C. & Berg, H. C. Visualization of flagella during bacterial
1154 swarming. *J. Bacteriol.* **192**, 3259–3267 (2010).

1155 67. Datsenko, K. A. One-step inactivation of chromosomal genes in Escherichia coli K-12
1156 using PCR products. *Proc. Natl. Acad. Sci.* **97**, 6640–6645 (2000).

1157 68. Plank, M., Wadhams, G. H. & Leake, M. C. Millisecond timescale slimfield imaging and
1158 automated quantification of single fluorescent protein molecules for use in probing
1159 complex biological processes. *Integr. Biol. (Camb).* **1**, 602–612 (2009).

1160 69. Ross, S. M. *A first course in probability*. (Pearson, 2013).

1161 70. Wilcox, R. R. *Comparing Two Independent Groups*. *Applyinf Contemporary Statistical*
1162 *Techniques* (2003). doi:10.4324/9781410613707-10

1163 71. Wang, F. *et al.* Non-equilibrium effect in the allosteric regulation of the bacterial flagellar
1164 switch. *Nat. Phys.* **13**, 710–714 (2017).

1165

1166

Figures

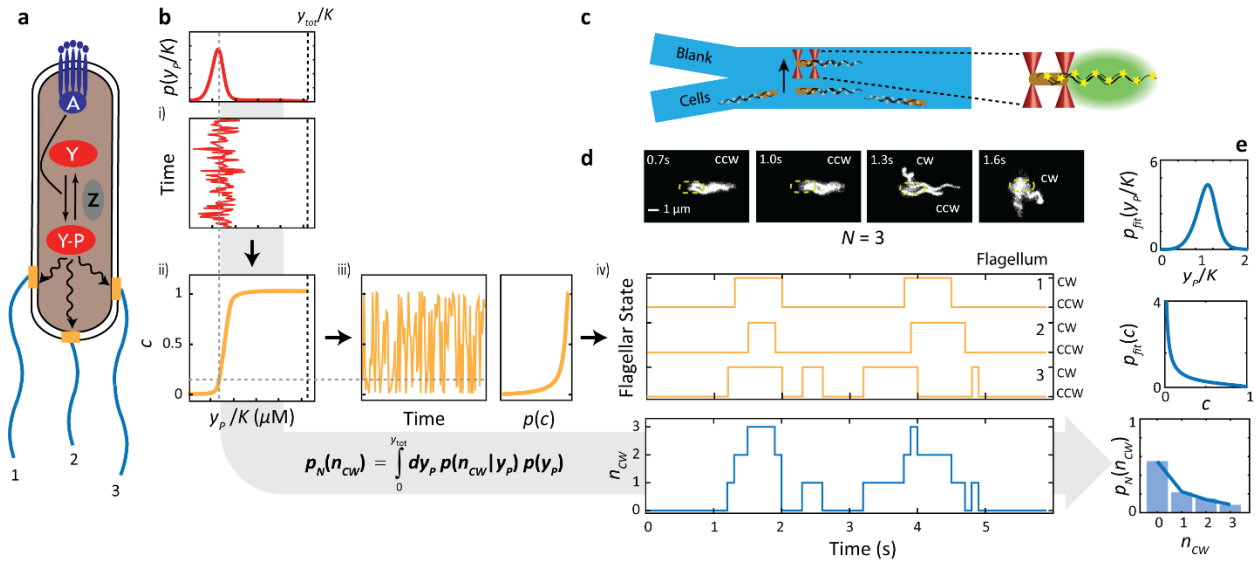

Figure 1. Estimating the temporal [CheY-P] distribution from flagellar dynamics of single *E. coli* cells. a. Schematic of a multi-flagellated *E. coli* cell showing key reactions of the chemotaxis signaling network. CheY is phosphorylated to CheY-P by the receptor kinase complex (CheA; dark blue); CheY-P is dephosphorylated by the phosphatase CheZ (gray). CheY-P binding to flagellar motors (mustard) causes a switch from CCW to CW rotation, which leads to cell tumbling. **b.** Temporal fluctuations in [CheY-P] due to chemotaxis network dynamics and their effect on flagellar switching statistics. i) [CheY-P] temporal fluctuations and corresponding distribution function $p(y_p)$. ii) Switch-like response of motor CW bias, c, to [CheY-P]. iii) Resulting temporal fluctuations in motor bias $c(t)$ and distribution of motor bias $p(c)$. iv) CCW/CW rotation state of three flagellar motors corresponding to the instantaneous motor bias c. The [CheY-P] distribution function $p(y_P)$ is directly related to the probability distribution $p_N(n_{CW})$ that n_{CW} out of N flagella rotate CW through the integral Eq. (4) (large gray arrow). **c.** Schematic of two-channel laminar flow chamber for optical trap assay. A single cell with fluorescently labelled flagella (gray stars) is captured from the bottom channel ("Cells"), aligned along the flow between two optical traps (red cones), moved to the upper channel ("Blank"), and its fluorescent flagella (yellow stars) imaged by stroboscopic slim-field microscopy (green). **d.** Fluorescence data trace from representative trapped cell with N = 3 flagella. Top, still images of fluorescent flagella, with

1186 position of the unlabeled cell body approximately indicated by the dashed yellow line. CW and
1187 CCW rotating flagella are labelled where clearly visible. Middle, CCW/CW rotation state of each
1188 flagellum vs. time (mustard). Bottom, corresponding number n_{CW} of CW flagella vs. time (light
1189 blue). **e**. Bottom, probability distribution $p_N(n_{\mathrm{CW}})$, determined experimentally from d (light blue
1190 bars) and fit (solid blue line) based on the model in Eq. (4). Middle, best fit estimate of the motor
1191 bias probability distribution $p_{fit}(c)$. Top, best fit estimate of the [CheY] probability distribution
1192 $p_{fit}(y_P)$.

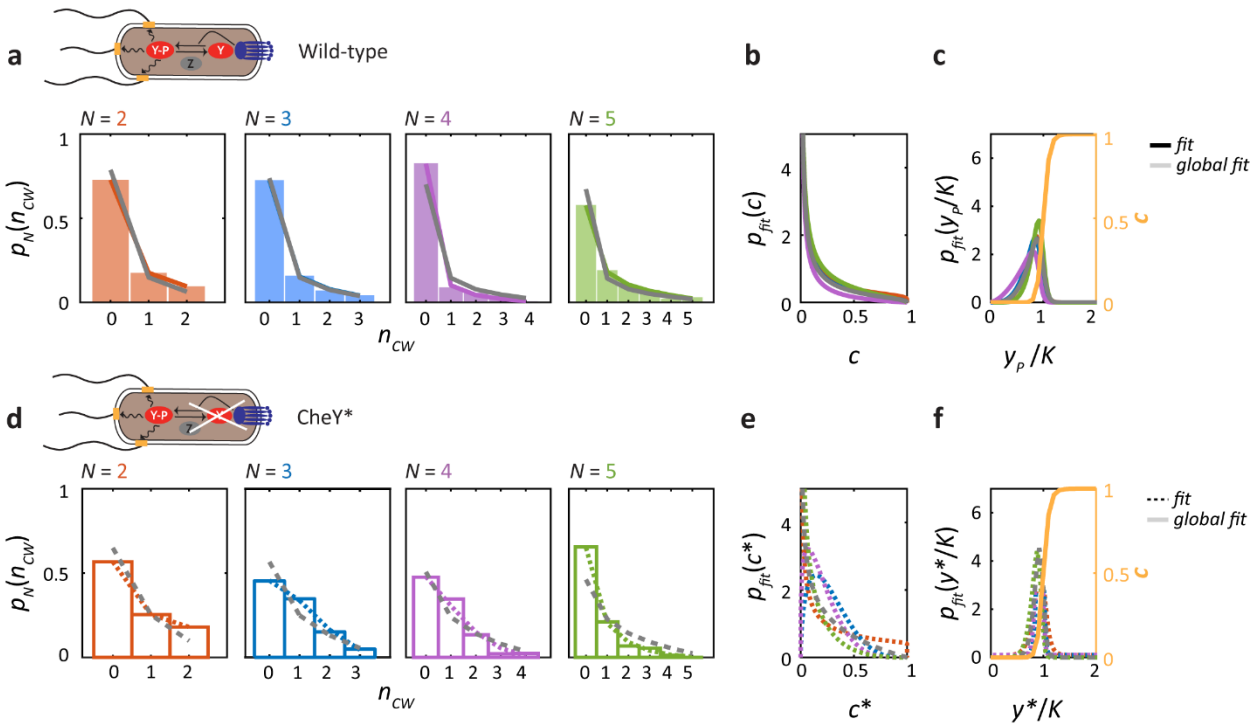

Figure 2. [CheY-P] fluctuations in the chemotaxis network at steady state. Measurement of flagellar dynamics and estimation of [CheY-P] fluctuations in wild-type *E. coli* strain HCB1660 (a-c) and in "CheY*" mutant strain PM87 expressing constitutively active CheY^{D13K} (d-f). **a.** Experimentally determined probability distribution $p_N(n_{CW})$ that n_{CW} out of N flagella rotate CW, grouped by cells with the same total number of flagella N = 2, 3, 4, 5 (number of cells = 13, 15, 14, 9 respectively). Best fit distributions $p_{N,fit}(n_{CW})$ determined separately for each N (colored solid lines) as well as globally (gray solid lines) are overlaid with the observed distributions (colored filled bars). **b.** Best fit probability distributions of the motor bias, $p_{fit}(c)$, determined separately for each N (colored solid curves) and globally (gray solid curve). **c.** Best fit probability distributions of [CheY-P], $p_{fit}(y_P)$, determined separately for each N (colored solid curves) and globally (gray solid curves) overlaid with Eq. (3), the relationship between motor bias c and y_P. **d-f.** Same as a-c for CheY* strain, showing experimental (open bars) and best fit (dashed lines and curves) distributions, grouped by cells with the same total number of flagella N = 2, 3, 4, 5 (number of cells = 13, 13, 9, 9 respectively).

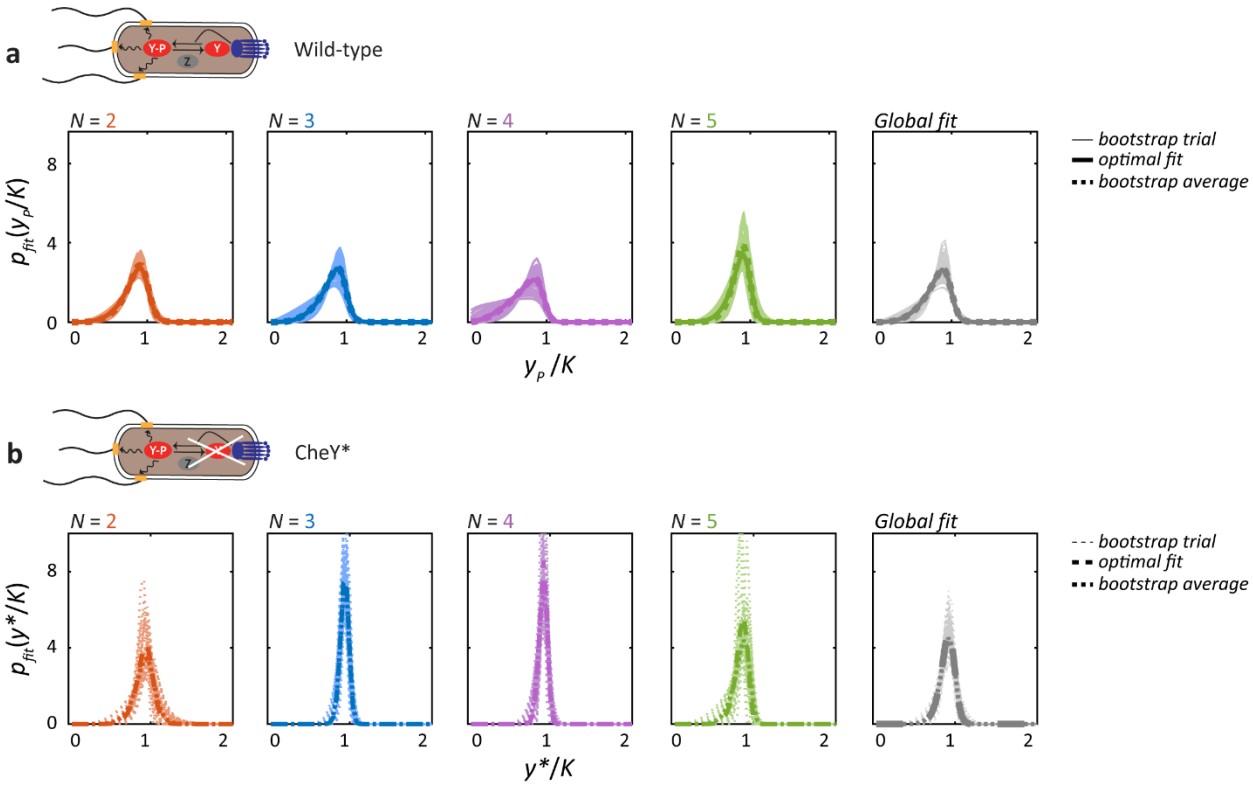

Figure 2 – figure supplement 1. Error in the estimated [CheY-P] probability distribution at steady state. a. Best fit [CheY-P] distribution $p_{fit}(y_P)$ for wild-type *E. coli* strain HCB1660 (thick colored curves) overlaid with each bootstrap resampling trial (thin colored curves) used to estimate the error and with the average over all bootstrap trials (thick dotted curve). Distributions determined for cells with the same total number of flagella N = 2, 3, 4, 5 as well as globally. **b.** Same as a for the "CheY*" mutant strain PM87.

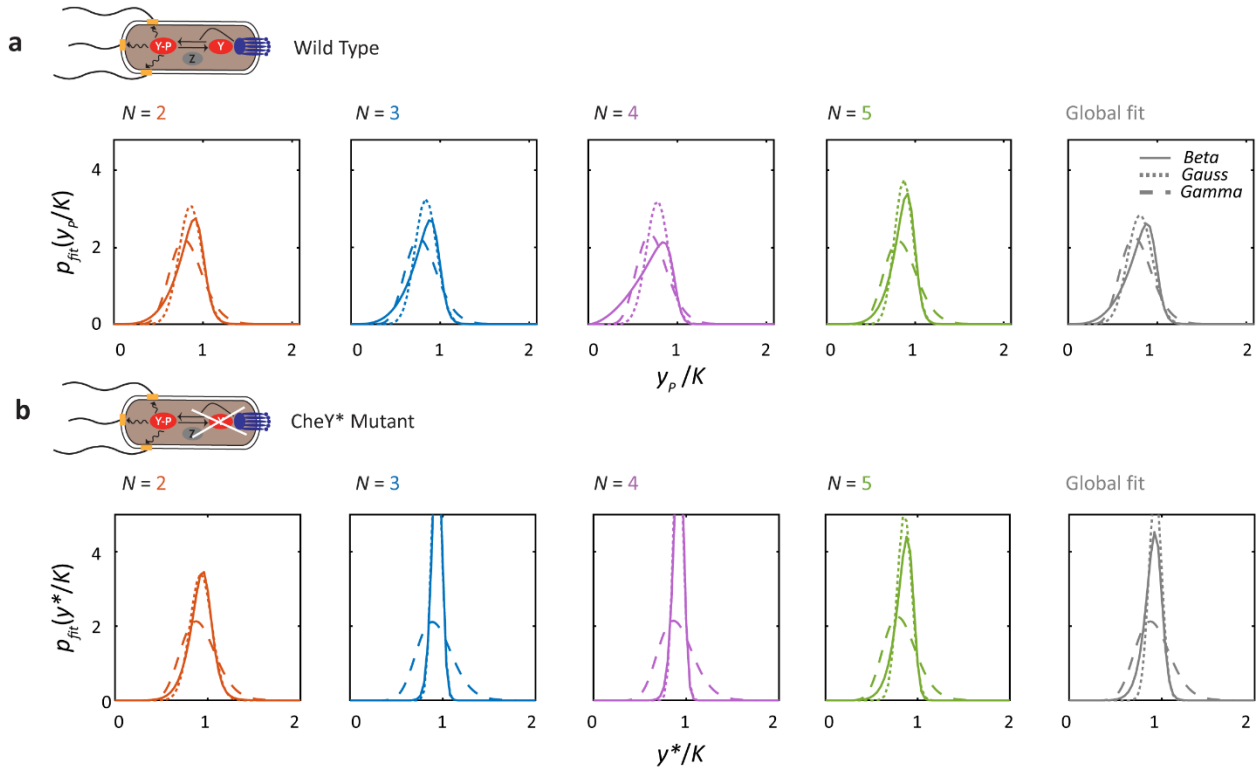

Figure 2 – figure supplement 2. Comparison of different trial functions for estimating the best fit [CheY-P] distribution. a. Best fit [CheY-P] distribution $p_{fit}(y_P)$ for wild-type *E. coli* with beta (solid curve), Gaussian (dotted curve) and gamma (dashed curve) distribution trial functions. Distributions determined for cells with the same total number of flagella N = 2, 3, 4, 5 as well as globally. **b.** Same as a for the CheY* mutant strain.

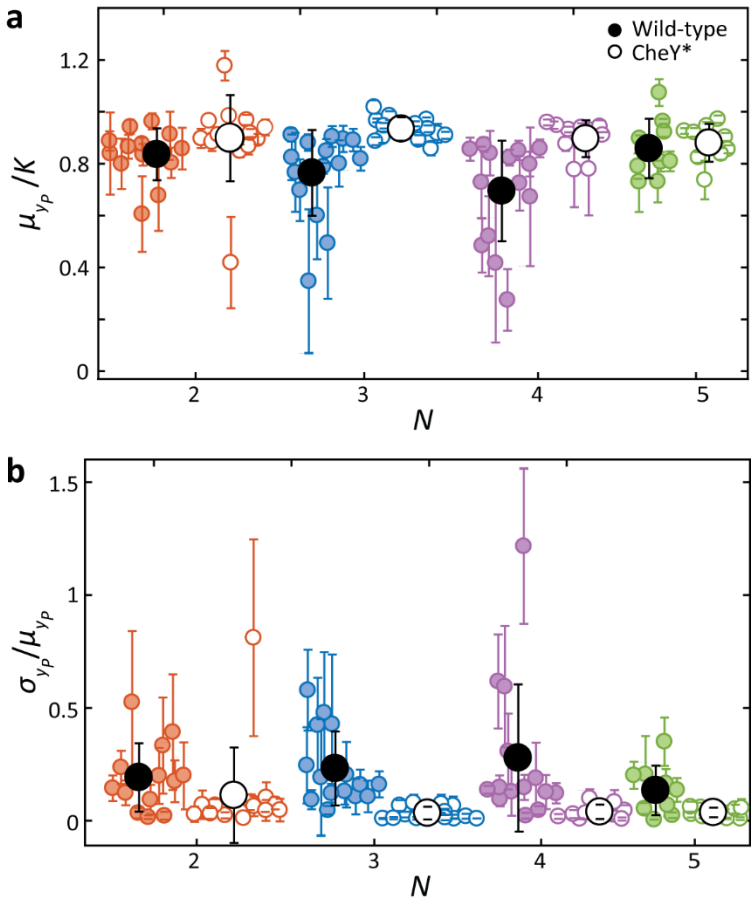

Figure 3. Estimate of the mean and coefficient of variation of [CheY-P] in individual cells. a. Comparison of mean relative [CheY-P], μ_{y_p}/K, determined for individual wild-type (colored circles) and CheY* cells (open circles), for different number of flagella *N*. **b.** Comparison of the coefficient of variation in [CheY-P], σ_{y_p}/μ_{y_p}, determined for individual wild-type (colored circles) and CheY* cells (open circles), for different *N*. Averages over each cell population are overlaid (black solid circles for wild-type, black open circles for CheY*); error bars represent standard deviation.

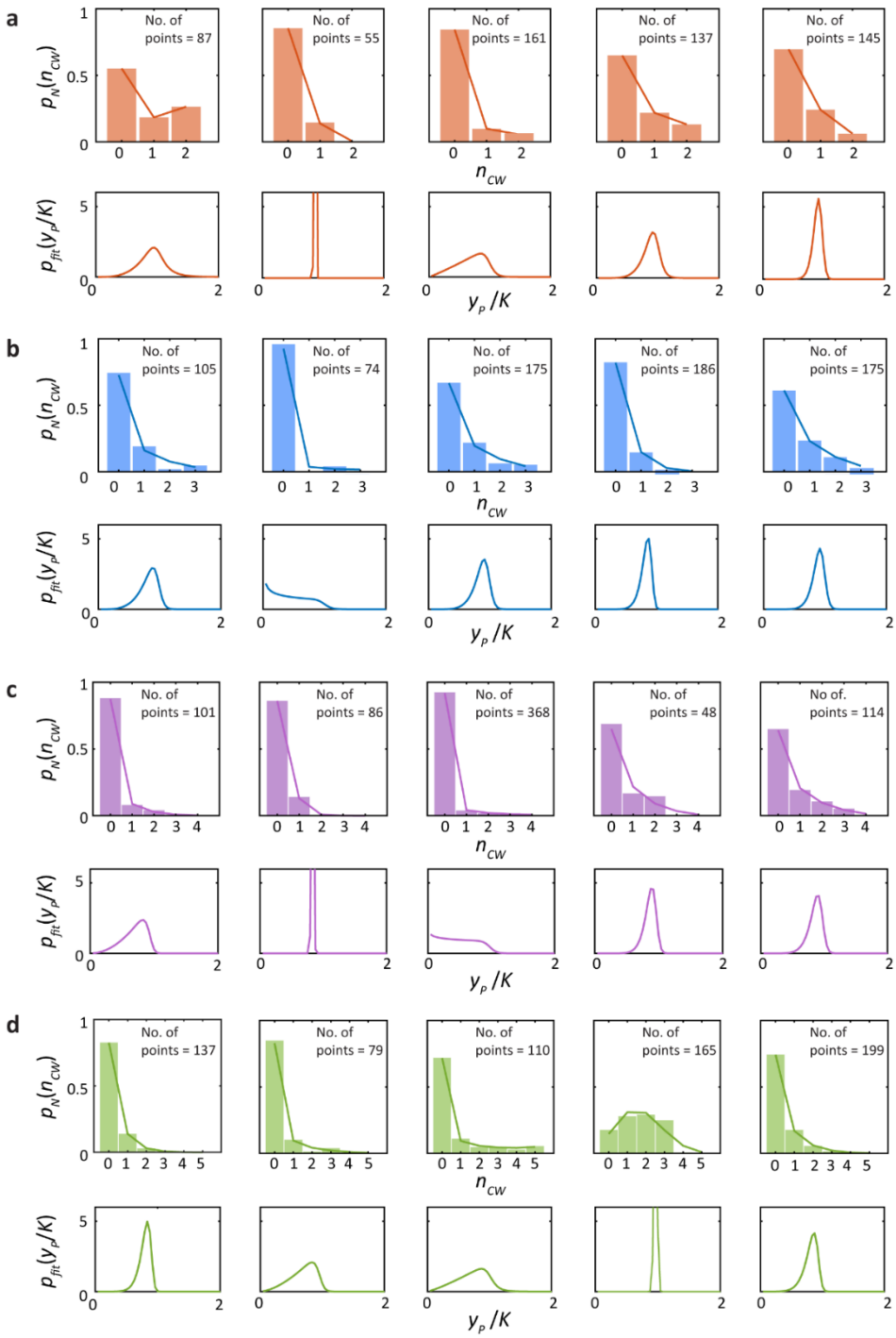

Figure 3 – figure supplement 1. [CheY-P] fluctuations in individual wild type *E. coli* cells. a. Top, experimentally determined probability distribution $p_N(n_{CW})$ (filled bars) and best fit $p_{N,fit}(n)$ (solid lines) for 5 individual representative cells with N = 2 flagella. Bottom, corresponding best fit [CheY-P] distribution $p_{fit}(y_P)$ (solid curves). **b-d.** Same as a, for N = 3, 4, and 5, respectively.

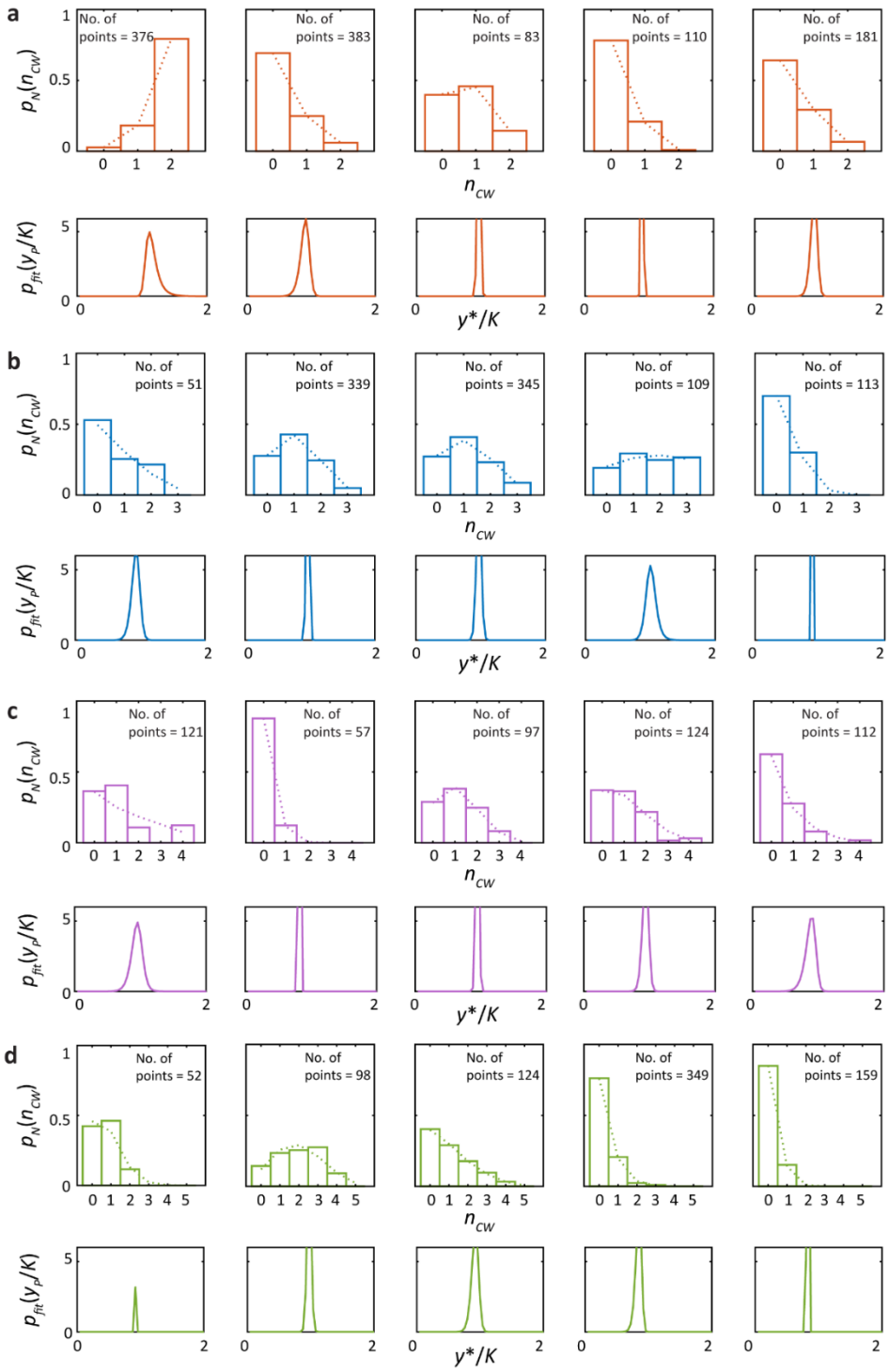

1233

1234 **Figure 3 – figure supplement 2. [CheY-P] fluctuations in individual mutant *E. coli* CheY* cells. a.**

1235 Top, experimentally determined probability distribution $p_N(n_{CW})$ (open bars) and best fit $p_{N,fit}(n)$

1236 (dashed lines) for 5 individual representative cells with N = 2 flagella. Bottom, corresponding best

1237 fit [CheY-P] distribution $p_{fit}(y^*)$ (dashed curves). **b-d.** Same as a, for N = 3, 4, and 5, respectively.

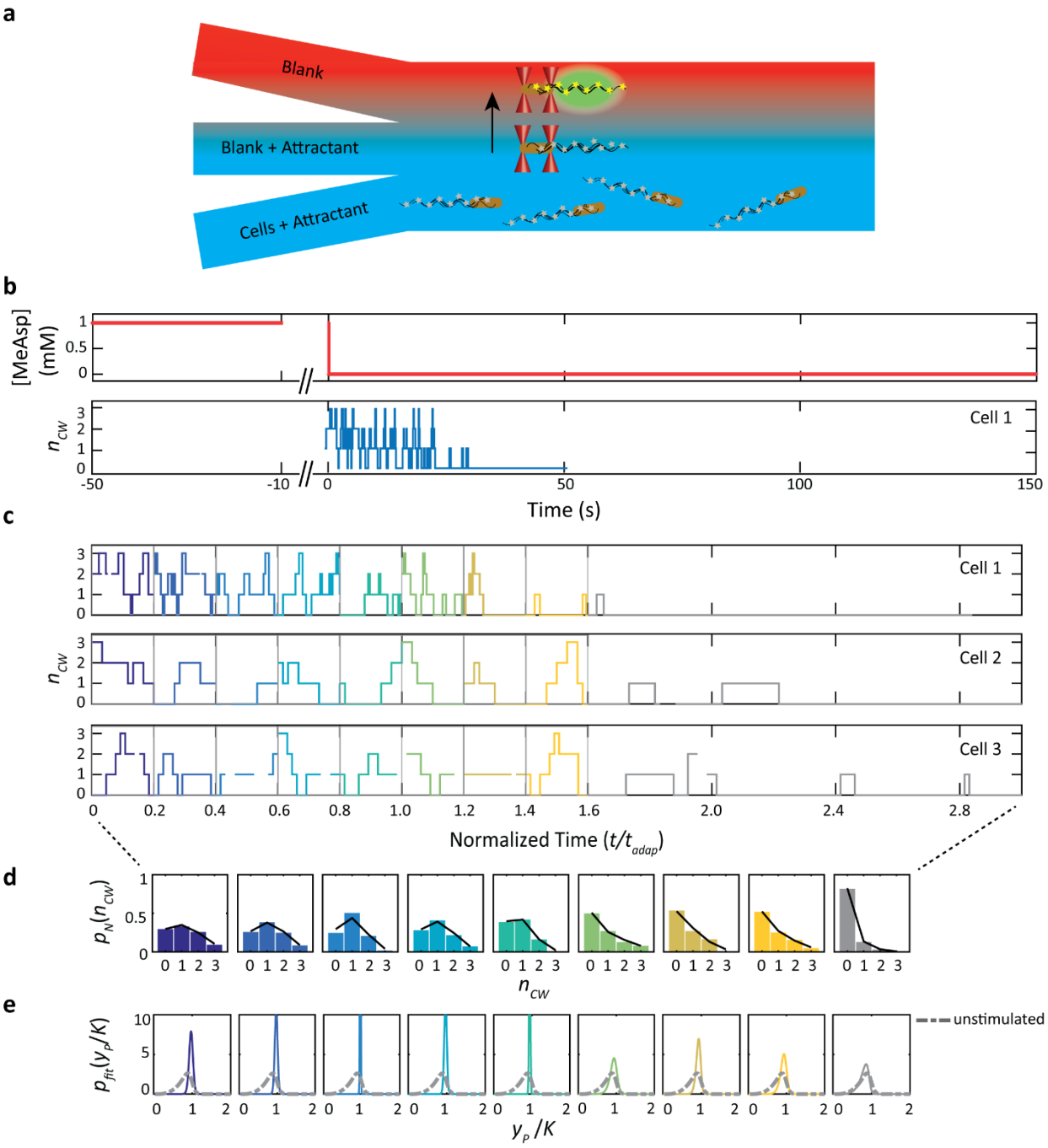

Figure 4. [CheY-P] fluctuations in the chemotaxis network upon stimulation. a. Schematic of three-channel laminar flow chamber for flagellar imaging of a cell experiencing a step down in attractant concentration. A single cell with fluorescently labelled flagella (gray stars) is captured from the bottom channel containing 1 mM MeAsp ("Cells + Attractant") and aligned along the flow between two optical traps (red cones) in the middle channel ("Blank + attractant"). The

1244 trapped cell is then moved to the upper channel lacking MeAsp ("Blank") and its fluorescent
1245 flagella (yellow stars) are imaged (green). **b.** Representative trace showing the response of "Cell
1246 1" to a step-down stimulus. Top, schematic of MeAsp concentration over time, showing the step
1247 down from 1 to 0 mM at $t = 0$. Data are not collected during the move from the middle to the top
1248 channel. Bottom, number n_{CW} of CW flagella over time after $t = 0$. **c-e.** Estimation of the [CheY-P]
1249 distribution in cells responding to a step-down stimulus. **c.** Traces from three representative
1250 "Cells 1, 2, 3" showing the number n_{CW} of CW flagella vs. time (normalized by each cell's
1251 adaptation time t_{adap}). Each trace is subdivided into windows of duration $0.2t_{adap}$, and data from
1252 each window is pooled across cells (for $N = 3$ flagella shown here, number of cells = 9). **d.**
1253 Distributions of the number of CW flagella $p_N(n_{\mathrm{CW}})$ for each window (colored bars) with the
1254 calculated best fits (black solid lines). **e**. Best fit [CheY-P] distributions, $p_{fit}(y_P)$, (colored curves)
1255 for each window. The [CheY-P] distribution for unstimulated cells is overlaid (gray dotted curve).

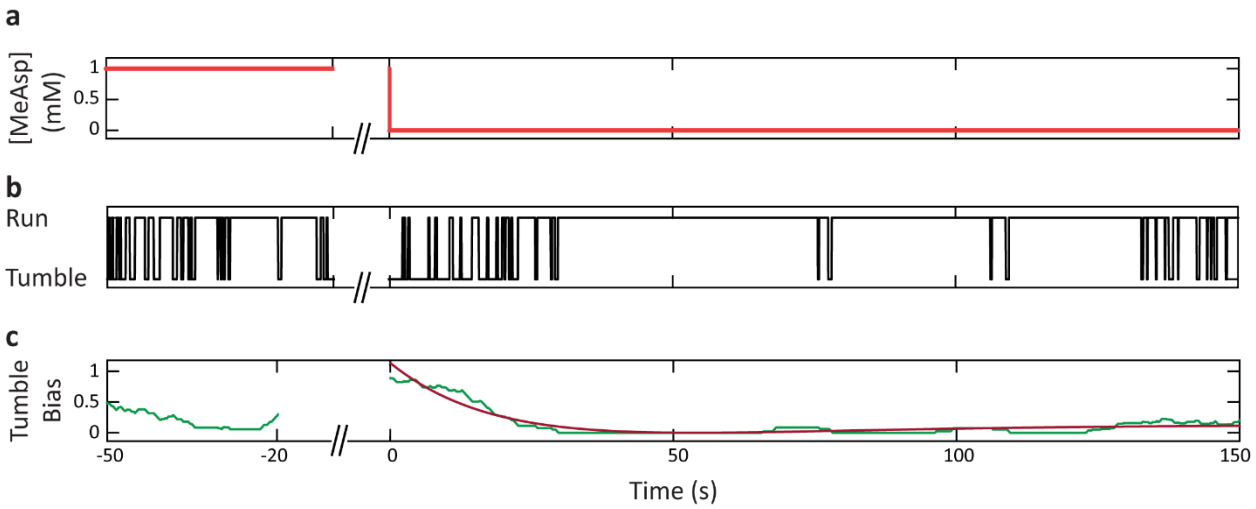

Figure 4 – figure supplement 1. Run-tumble response of a cell to a step-down stimulus. a. Schematic of MeAsp concentration over time, showing the step down from 1 to 0 mM at $t = 0$. **b.** Run-tumble binary time trace of a representative cell. Data are not collected during the move from the middle to the top channel. **c.** Tumble bias of the cell (green), determined at each time point from the fraction of time tumbling over a 10-s moving window, and fit to bi-exponential function (red) Eq. (16).

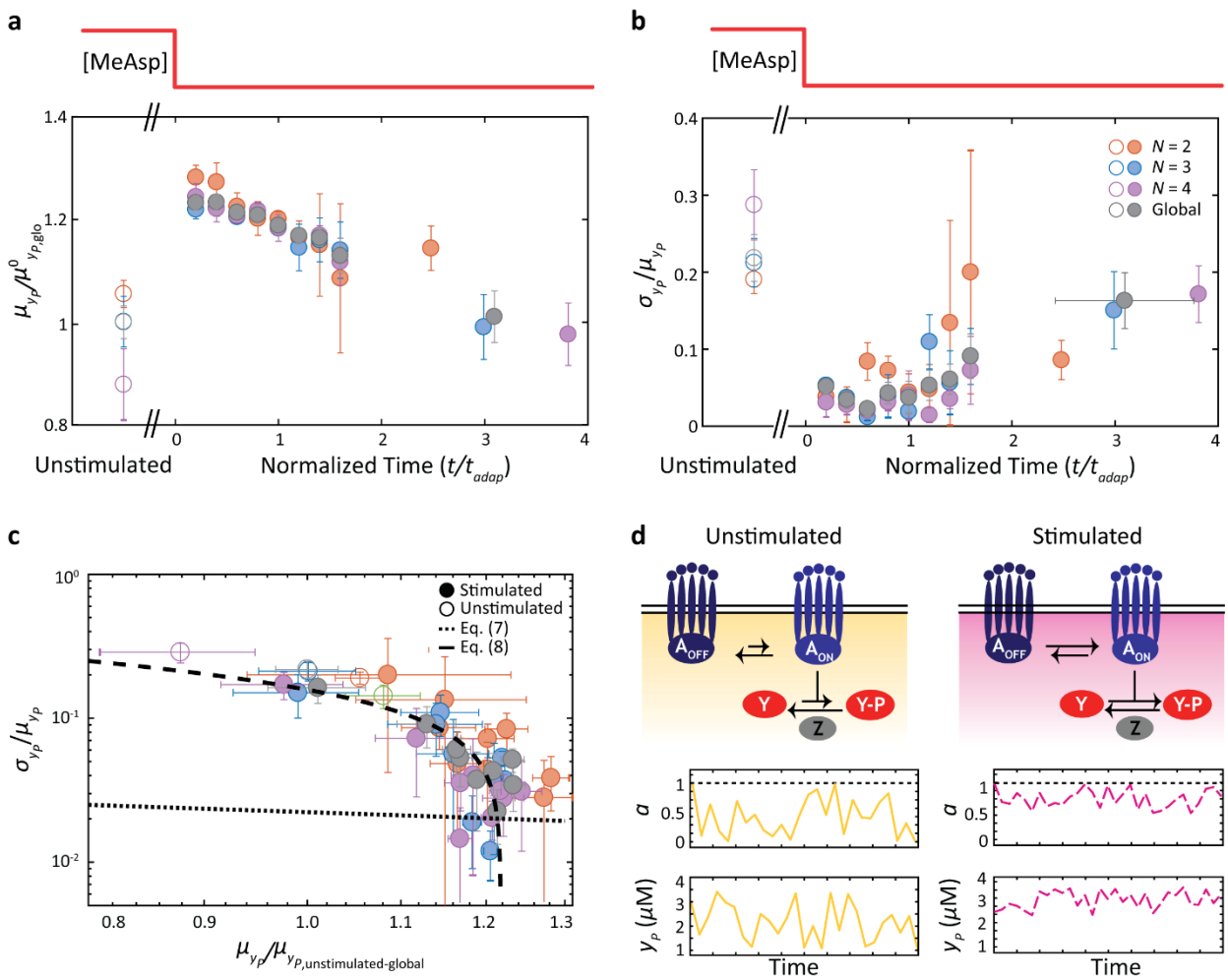

Figure 5. Reduction in [CheY-P] fluctuations post stimulus due to kinase phosphorylation dynamics. a. Mean [CheY-P], μ_{y_p}, vs. normalized time t/t_{adap} after step down stimulus (top schematic, red) determined separately for each number of flagella N (colored circles) and globally (gray circles). μ_{y_p} is normalized by the global best fit mean [CheY-P] for unstimulated cells, $\mu^0_{y_p,\mathrm{glo}}$. **b.** Coefficient of variation in [CheY-P], σ_{y_p}/μ_{y_p}, after step down. Same color code as a. Data are pooled by cells with the same total number of flagella N = 2, 3, 4 (number of cells = 9, 9, 9). The pre-stimulus mean and coefficient of variation in [CheY-P] were obtained from the analysis of the unstimulated cells in Fig. 2. **c.** Coefficient of variation in [CheY-P], σ_{y_p}/μ_{y_p}, plotted against the normalized mean [CheY-P], $\mu_{y_p}/\mu^0_{y_p,\mathrm{glo}}$, for data from unstimulated and stimulated cells from a and b. Fits to Eq. (7) and Eq. (8) are also shown. **d.** Simple model of [CheY-P] fluctuations in the *E. coli* cell. (Left) In unstimulated cells, the fluctuations in CheA activity at the steady state lead

1275 to CheY-P production in bursts. (Right) In stimulated cells, CheA activity is higher on average than
1276 in unstimulated cells and shows reduced fluctuations as it approaches the kinetic ceiling. This
1277 also causes a reduction in [CheY-P] fluctuations at high mean [CheY-P].

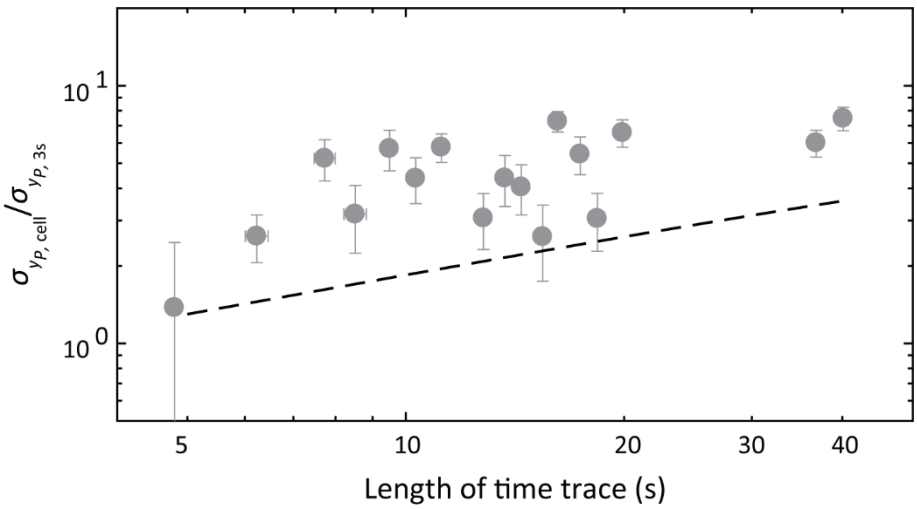

Figure 5 – figure supplement 1. Dependence of [CheY-P] noise estimates on data time window duration. Ratio of standard deviation in [CheY-P] estimated over an entire single-cell trace to the standard deviation estimated over 3-s windows of the same trace, $\sigma_{y_p,\mathrm{cell}}/\sigma_{y_p,3\mathrm{s}}$, plotted vs. trace duration (gray filled circles). Data globally fitted from cells with different numbers of flagella. The noise estimates increase with trace duration, a trend replicated by a simple model (black dotted line). The model assumes that the spectral density in [CheY-P] is given by a Lorentzian with characteristic timescale τ_A = 12.6 s (see Ref. (33)). Integrating the spectral density yields an expression for the standard deviation, $\sigma_{y_p} = \frac{c\tau_A}{\pi}(\tan^{-1}(2\pi\tau_A f_{high}) - \tan^{-1}(2\pi\tau_A f_{low}))$, in terms of the data bandwidth. f_{high} = 10 Hz is the sampling rate and f_{low} = 1/trace duration. c is a constant.

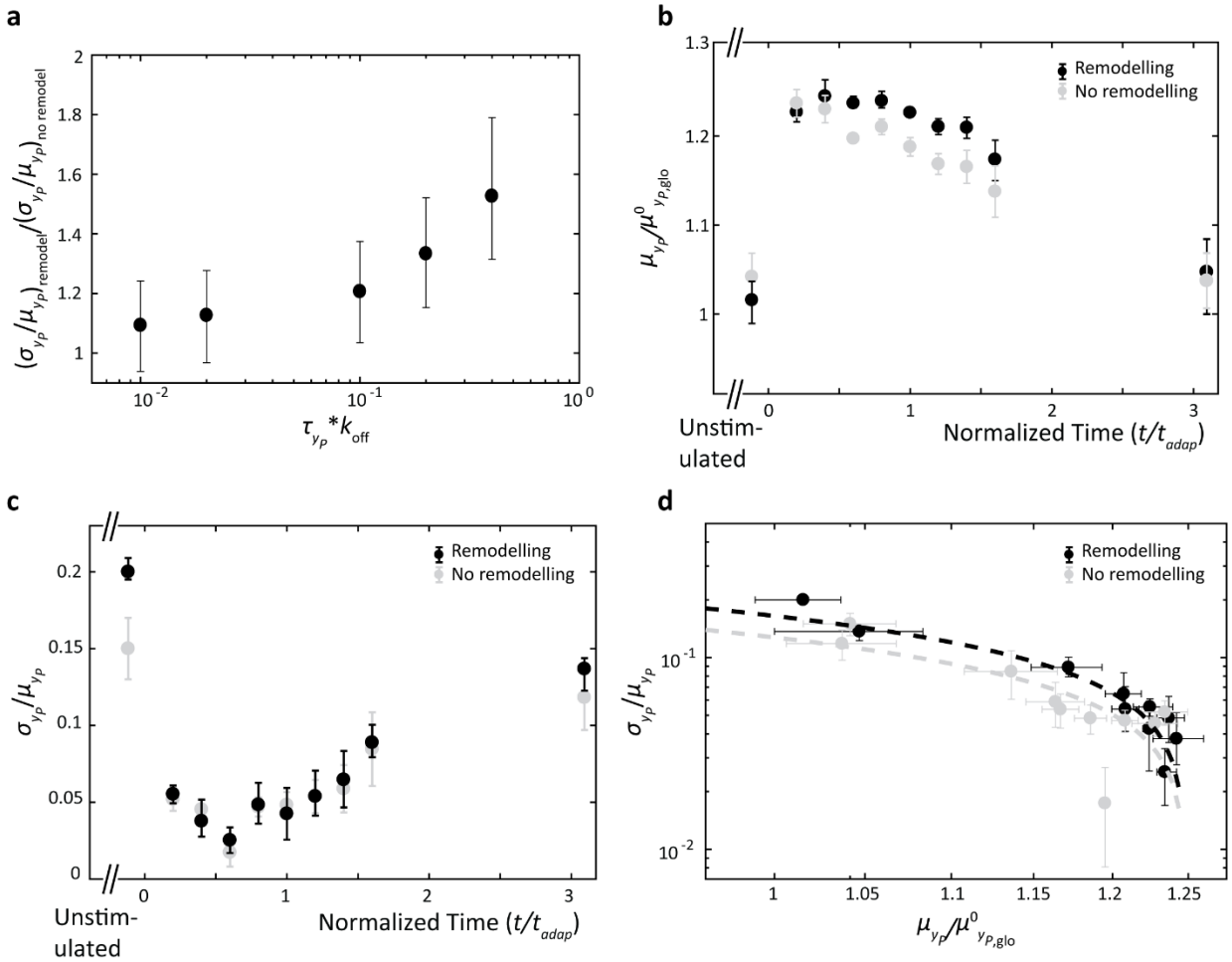

Appendix – figure 1. The effect of flagellar motor remodeling on CheY-P fluctuation estimates. **a.** Coefficient of variation in [CheY-P], σ_{y_p}/μ_{y_p}, from simulations accounting for flagellar motor remodeling vs. CheY-P fluctuation timescale τ_A. σ_{y_p}/μ_{y_p} is normalized by the coefficient of variation without motor remodeling, and τ_A is normalized by the motor remodeling rate k_{off}. **b.** Mean [CheY-P] μ_{y_p} vs. normalized time t/t_{adap}, taking into account flagellar motor remodeling (black) and ignoring remodeling (light gray). μ_{y_p} is normalized by the global best fit mean [CheY-P] without remodeling, $\mu^0_{y_p,\mathrm{glo}}$. **c.** Same as b, for the coefficient of variation in [CheY-P], σ_{y_p}/μ_{y_p}. **d.** Coefficient of variation in [CheY-P] σ_{y_p}/μ_{y_p} vs. normalized mean [CheY-P], $\mu_{y_p}/\mu^0_{y_p,\mathrm{glo}}$ from b and c. Data points are normalized as in Fig. 5a-c. Simulations are based on globally fitted experimental data in Fig. 5a-c. Simulations in b-d assume a CheY-P fluctuation timescale τ_A = 10 s (see Appendix).